GEORGIA INSTITUTE OF TECHNOLOGY
OFFICE OF CONTRACT ADMINISTRATION
SPONSORED PROJECT INITIATION

Date: 10-26-79

Project Title: Hybrid Dish-Stirling Solar Receiver Preliminary Design Program

Project No: A-2348

Project Director: Dr. Steve H. Bomar, Jr.

Sponsor: Fairchild Stratos Division; Manhattan Beach, California 90266

Agreement Period: From 3/23/79 Until 9/30/79

Type Agreement: Purchase Order No. F-E0064 (subcontract under NAST-100)

Amount: $ 33,706.03 authorized
(checks received for $41,555.88)

Reports Required: Engineering Report

Sponsor Contact Person (s):

Technical Matters

Mr. Lon Isenberg
Fairchild Stratos Division
1800 Rosecrans Avenue
Manhattan Beach, California
90266

Contractual Matters
(thru OCA)

Mr. Patrick Moore, Buyer
Fairchild Stratos Division
1800 Rosecrans Avenue
Manhattan Beach, California
90266 (213) 675-9111

Defense Priority Rating: None

Assigned to: ERL/SRB (School/Laboratory)

COPIES TO:

Project Director
Division Chief (EES)
School/Laboratory Director
Dean/Director–EES
Accounting Office
Procurement Office
Security Coordinator (OCA)
Reports Coordinator (OCA)

Library, Technical Reports Section
EES Information Office
EES Reports & Procedures
Project File (OCA)
Project Code (GTRI)
Other

CA–3 (3/76)

GEORGIA INSTITUTE OF TECHNOLOGY
OFFICE OF CONTRACT ADMINISTRATION

SPONSORED PROJECT TERMINATION

Date: November 21, 1979

Project Title: Hybrid Dish-Stirling Solar Receiver Preliminary Design Program

Project No: A-2348

Project Director: Dr. Steve H. Bomar, Jr.

Sponsor: Fairchild Stratos Division; Manhattan Beach, California 90266

Effective Termination Date: 9/30/79

Clearance of Accounting Charges: 9/30/79

Grant/Contract Closeout Actions Remaining:

X Final Invoice ~~and Closing Documents~~

_ Final Fiscal Report

_ Final Report of Inventions

_ Govt. Property Inventory & Related Certificate

_ Classified Material Certificate

_ Other _____

TERMINATED

Assigned to: ERL/SRB (School/Laboratory) XXXXX

COPIES TO:

Project Director
Division Chief (EES)
School/Laboratory Director
Dean/Director–EES
Accounting Office
Procurement Office
Security Coordinator (OCA)
Reports Coordinator (OCA) ✓

Library, Technical Reports Section
EES Information Office
Project File (OCA)
Project Code (GTRI)
Other _____

CA–4 (1/79)

PRELIMINARY DESIGN REPORT

PROJECT A-2348

DISH STIRLING SOLAR RECEIVER PRELIMINARY DESIGN REPORT

By

S. H. Bomar, Jr.
R. D. Chelf
T. B. Elfe

June 1979

Prepared for

Fairchild Stratos Division
Manhattan Beach, CA 90266

Engineering Experiment Station
Georgia Institute of Technology
Atlanta, Georgia 30332

2.4 OPTICAL ANALYSIS

A computer model for optical analysis was developed in order that the distribution of solar energy flux arriving at the receiver walls could be calculated. The calculation begins by considering a radial line along the surface of the parabolic collector dish. This line is divided into a number of points equally spaced in distance from the center line; typically, 600 points are used. A random slope error is chosen at each point, within the following constraints:

1. The magnitudes of the 600 slope errors have a normal distribution with a standard deviation, σ .
2. Care is taken to distribute the slope errors along the line so that all the small or large errors are not in the same radial region of the collector.
3. The direction of each slope error is random.

For each point on the collector surface, 13 rays are traced to find the coordinates (x, y, z) of the intersection of each ray with the receiver surface. The receiver surface of interest is specified by the user and may be a plate perpendicular to the collector axis, a cone whose axis coincides with the collector axis, or a cylinder whose axis coincides with the collector axis. The 13 rays represent energy received from areas on the solar disk:

1. The central area, subtending to angle $\leq$ 4 minutes of arc (one ray).
2. The area whose subtended angle is between 4 and 8 minutes (4 rays).

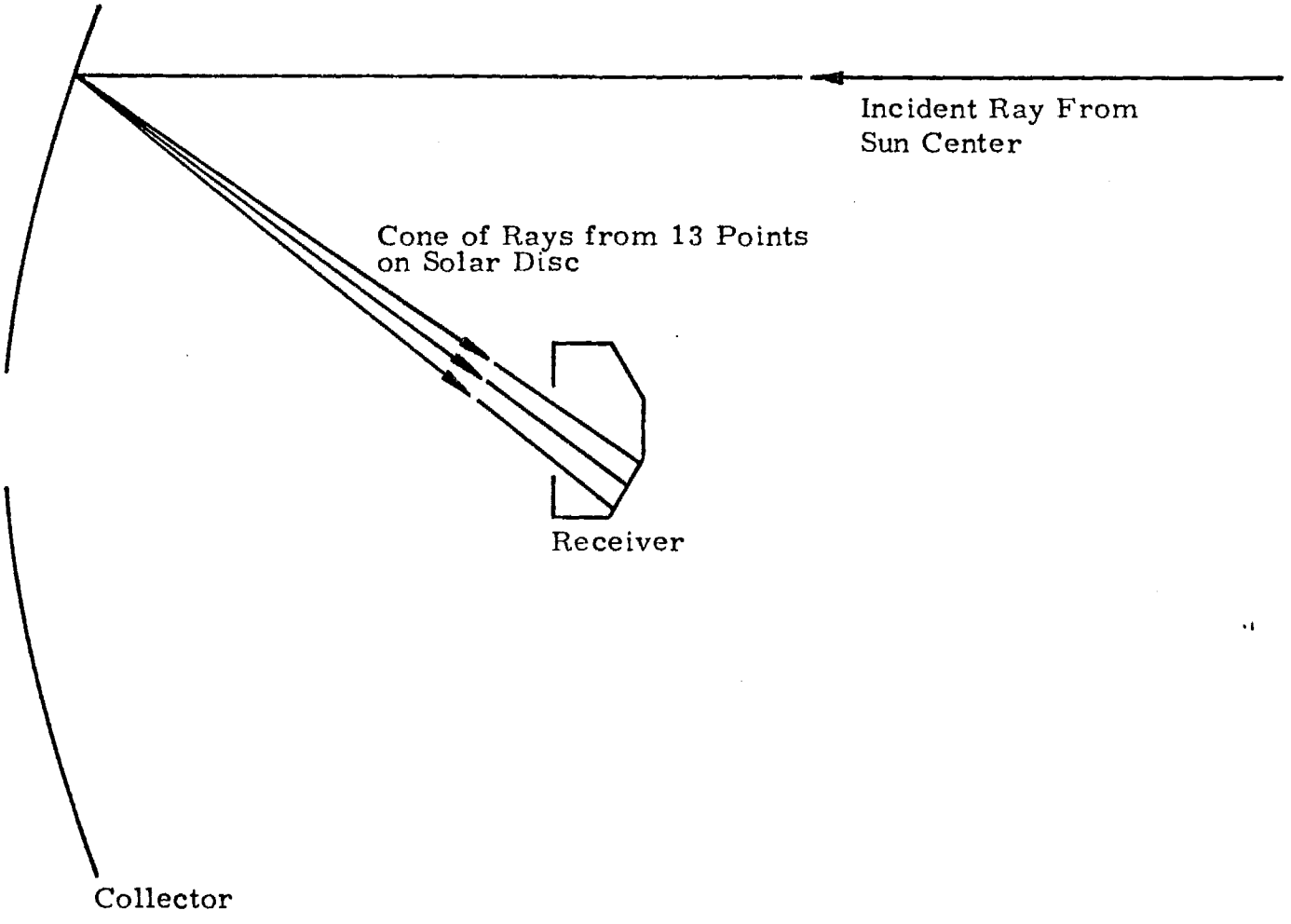

Figure 2-1. Optical Analysis Model

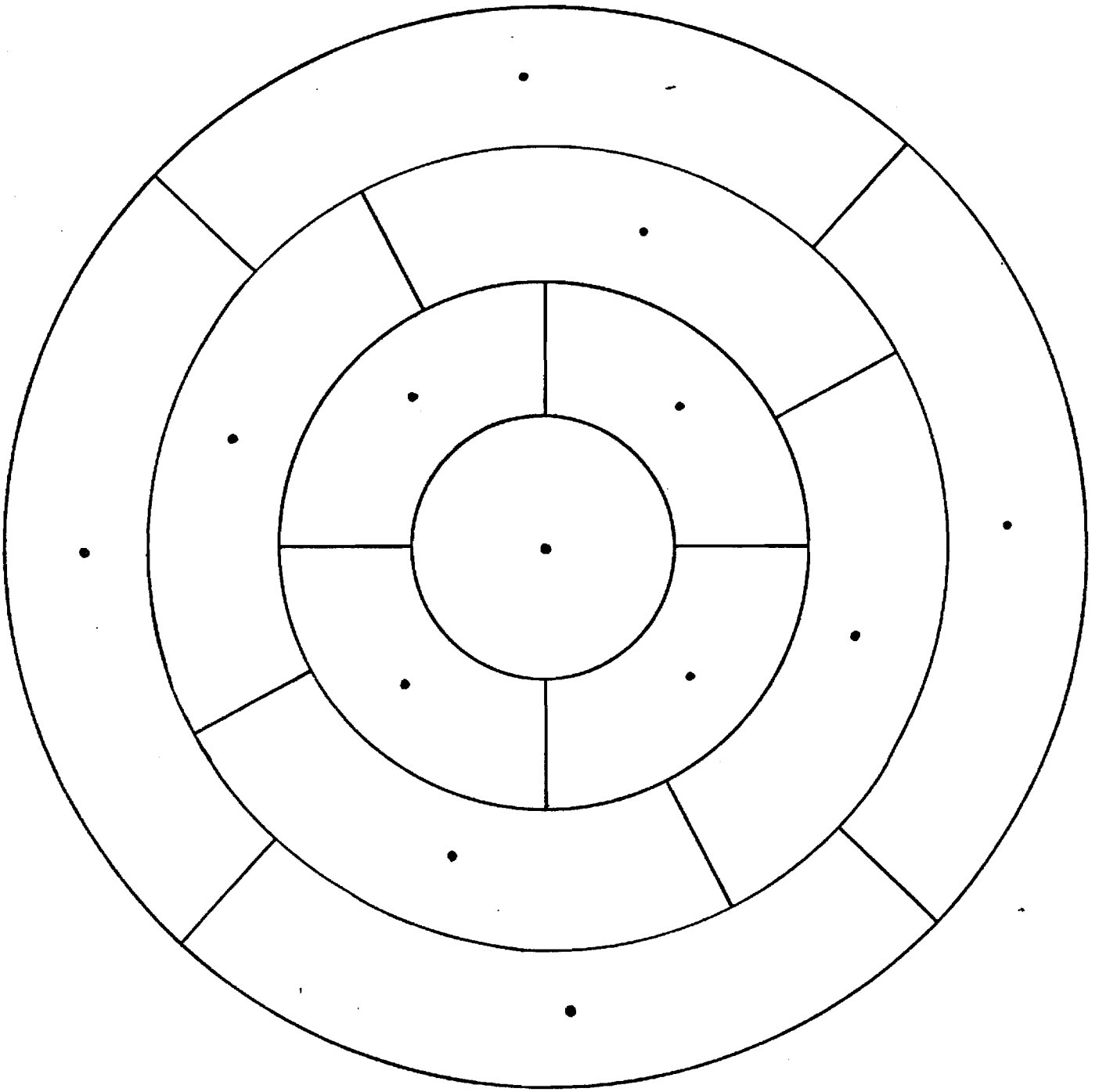

Figure 2-2. Sun Model

3. The area whose subtended angle is between 8 and 12 minutes (4 rays).
4. The area whose subtended angle is between 12 and 16 minutes (4 rays).

The origins of the rays representing rings on the solar disk are rotated randomly about the central ray, so that samples of energy from the entire sun are incorporated into the calculation. Each ray is weighted according to the area of the sun which it represents, the relative intensity of the sun at that radius, and the area normal to the central ray which the point on the collector surface represents. The sum of the ray weights is normalized to a user-supplied value of total power leaving the collector surface (67 kW in the present case).

The receiving surface, whether it is a plate, cone or cylinder, is divided into rings whose radial or axial width is selected by the user. The program sums the rays arriving at each ring on the receiving surface, taking into account the ray weights. The program outputs are flux density incident at the center of each ring and the total thermal power incident of each ring.

This computer model evolved from a program which was written to analyze the flux pattern at the Advanced Components Test Facility, a solar test facility operated by Georgia Tech for the Department of Energy. It was intended to supplement the HELIOS program developed by Sandia Laboratories for analysis of heliostat fields. The present program, known as OPTIK was designed for:

1. Interactive operation for quick and easy inspection of collectors.
2. Ability to handle flux patterns on a variety of receiving surfaces.

The agreement between computed and measured flux patterns at the ACTF has been very good. There are, however, several areas in which the program OPTIK could be further refined:

1. The outermost rays of the sun are represented by rays originating 14 minutes from the center of the solar disk. This causes some inaccuracy in defining the extreme edges of the flux pattern.
2. The assignment of perfectly random directions for slope errors leads to an imperfect correlation with other ray tracing programs being used for small solar power system designs, specifically that developed by Dr. Peter Poon of JPL. The JPL program permits independent assignment of radial and circumferential slope errors. OPTIK results correlated satisfactorily with JPL results, however, on a plate at the dish focal plane when the OPTIK slope errors were multiplied by the factor $4/\pi$.
3. 600 points on the collector surface is not really enough to give "smooth" results. For example, two rather large slope errors near the outside of the collector result in 26 rather heavily weighted rays missing the focal point by a fairly wide margin.

Work is still in progress to improve these features. However, we have a high level of confidence in the results shown in this report and believe they are entirely adequate for preliminary design calculations.

2.4.1 Methodology and Results

At the beginning of the program, several runs were made with 45 degree cones positioned at various axial distances from the focal plane of the dish collector. The results showed very high flux densities which were not uniformly distributed over those portions of the receiver surface adjacent to the helium flow passages. By varying cone angle and vertex location, it was found that an acceptable flux pattern would be produced on a 60 degree cone whose vertex was 0.373 meters from the focal plane.

JPL sent data for flux patterns on the flat plates for comparison with OPTIC runs at Georgia Tech. Satisfactory agreement on flat plate patterns was achieved by redefining the Georgia Tech interpretation of slope errors to more closely match the JPL definition; this required that the Georgia Tech values of slope error be multiplied by the factor $4/\pi$. Using the redefined slope error values, the 60 degree cone with a vertex at 0.373 meters still appeared to give near-optimum heat flux patterns.

The first thermal analysis runs were made with the flux pattern in a cone of this configuration and on an outer cylinder having a 9-inch radius. 2 milliradian slope error was used in these analyses.

It was then concluded that the most probable slope error would be 3 milliradians. We then made a series of optical analyses which are summarized in Table 2-2. These runs were made without consideration of aperture interception, but enabled us to reach the conclusion that:

1. Too high a percentage of total flux falls outside a 9-inch radius for 60-degree cones.
2. Peak flux density is too high on 45-degree cones.
3. .353 meter focal plane - vertex spacing gets most of the flux between 2.1-inch and 9-inch radius on 55-degree cones without resulting in excessive flux density.

Another comprehensive series of runs was made for 55 and 60-degree cones, with aperture sizes varying from 25 to 31 cm. Total errors varying from 2 to 4 milliradians, with outer cylinders at 9-inch and 11-inch radius. These optical runs were made primarily to set flux inputs for thermal analysis runs.

After thermal analysis had shown that the center plug is apt to be the hottest point in the receiver, several additional runs were made to see if increasing the diameter of the 1.2 meter hole in the collector would have a dramatic effect in reducing the flux falling inside the 2.1-inch radius at the center of the receiver. We found however that the central flux falls off rather slowly as hole diameter increases, so that increasing the collector hole size does not appear to be a reasonable solution.

Finally, the test bed concentrator was built into the optical analysis model. Individual facets were modelled by assuming the center of each facet to be correctly oriented and calculating

Table 2-2. Optical Analysis Summary

TOTAL ERROR	CONE ANGLE	VERTEX LOCATION	MAX. FLUX	R FOR MAX FLUX	% 2.1"	% 9"
2	60	.353	125.7×10^6	7 "	2.6	8.5
		.373	110.1	7	2.2	13.7
		.393	103.1	8	1.9	19.8
	55	.353	134.6	6	2.8	4.0
		.373	126.7	7	2.3	7.1
		.393	112.1	7	2.0	11.5
	45	.353	165.9	6	3.3	.3
		.373	153.8	6	2.8	.7
		.393	136.8	6	2.3	1.7
3	60	.353	115.6	6	3.1	11.7
		.373	106.2	7	2.7	16.6
		.393	96.5	7	2.3	22.6
	55	.353	125.4	6	3.2	6.4
		.373	113.5	6	2.8	10.3
		.393	108.0	7	2.4	14.5
	45	.353	148.3	5	3.8	1.4
		.373	134.8	6	3.2	2.1
		.393	128.5	6	2.8	3.5
4	60	.353	117.6	4	3.3	15.2
		.373	103.1	5	3.0	20.4
		.393	93.2	6	2.6	25.5
	55	.353	125.1	5	3.5	9.6
		.373	113.0	5	3.1	13.6
		.393	100.6	6	2.7	18.4
	45	.353	140.6	5	4.0	2.9
		.373	129.8	5	3.5	4.3
		.393	117.5	5	3.0	5.8

slope error based on spherical radius of the facets as a function of distance from facet center. In addition to this systematic slope error, a random slope error (still having normal distribution) was taken to be 0.5 milliradian X SQRT(2) (to include structure deflection. Figure 2-3 shows the result, which was also used to provide input for a thermal analysis of the TBC test.

To further summarize results, the effect of the cone angle and position, which have already been discussed in Table 2-2, are shown graphically in Figures 2-4 and 2-5. The change in flux pattern with cone position is rather slow and predictable. If the cone is moved closer to the focal plane, overall flux density increases and less flux hits the outer portion of the cone, while more flux hits the central plug. Cone angle has a more pronounced effect. The flux pattern becomes more uniform with lower flux density for a 60-degree cone, but there is too much flux in the area with no helium passages. Flux density becomes excessive for the 45-degree cone. The 55-degree cone appears to be the best compromise.

From the optical standpoint, the effects of aperture size are twofold. First, flux is intercepted on the aperture plate, which must be designed to withstand it. Figure 2-6 shows aperture interception as a function of aperture size and slope error. We should reiterate that the image size at the focal plane is slightly larger than our computer model predicts. The second effect of aperture size is to reduce the flux on the cylinder. This is illustrated in Figure 2-7.

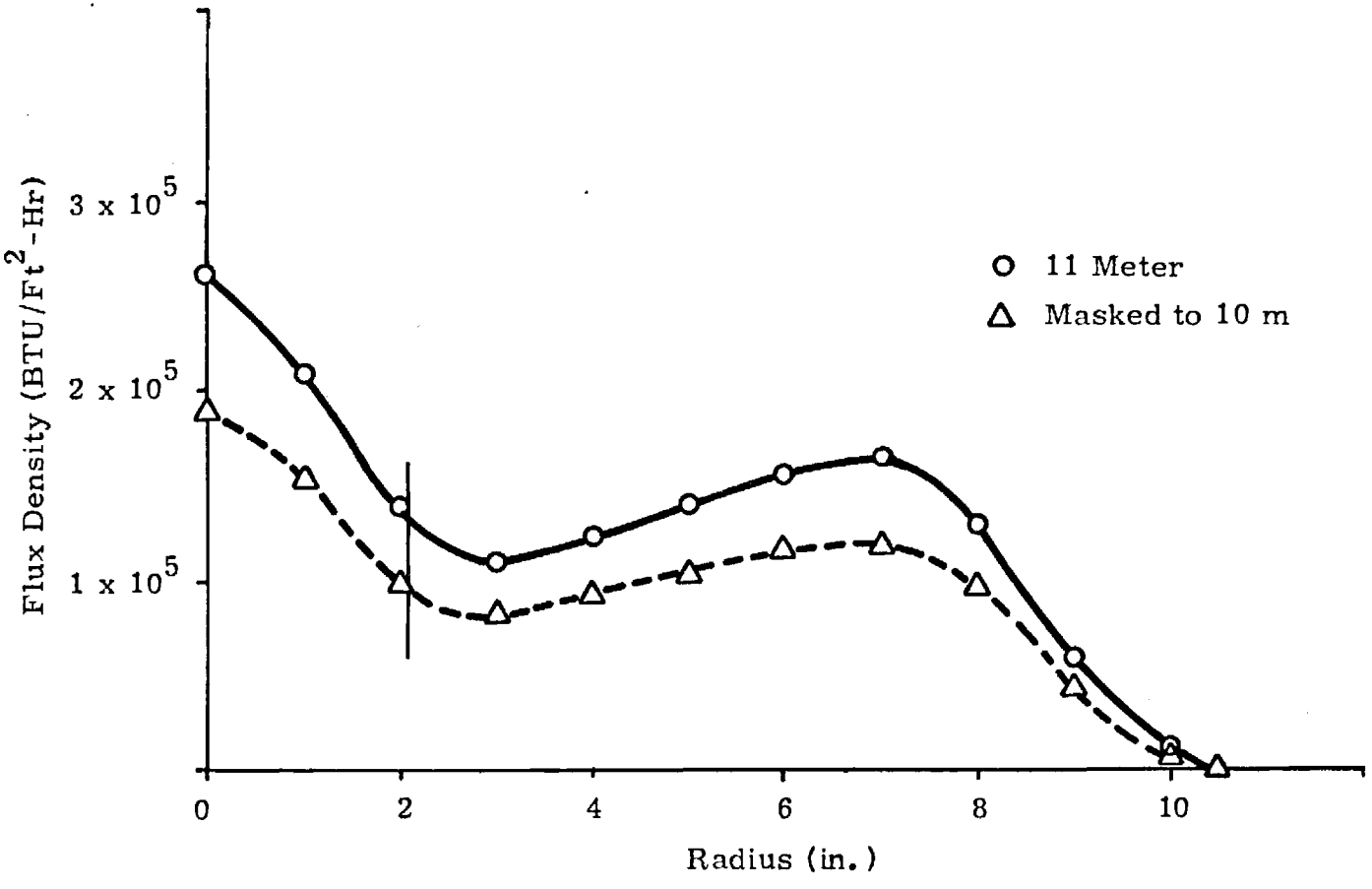

Figure 2-3. Flux Plot from Test Bed Concentrator on 55° Cone, Vertex 0.353 M from Focal Plane

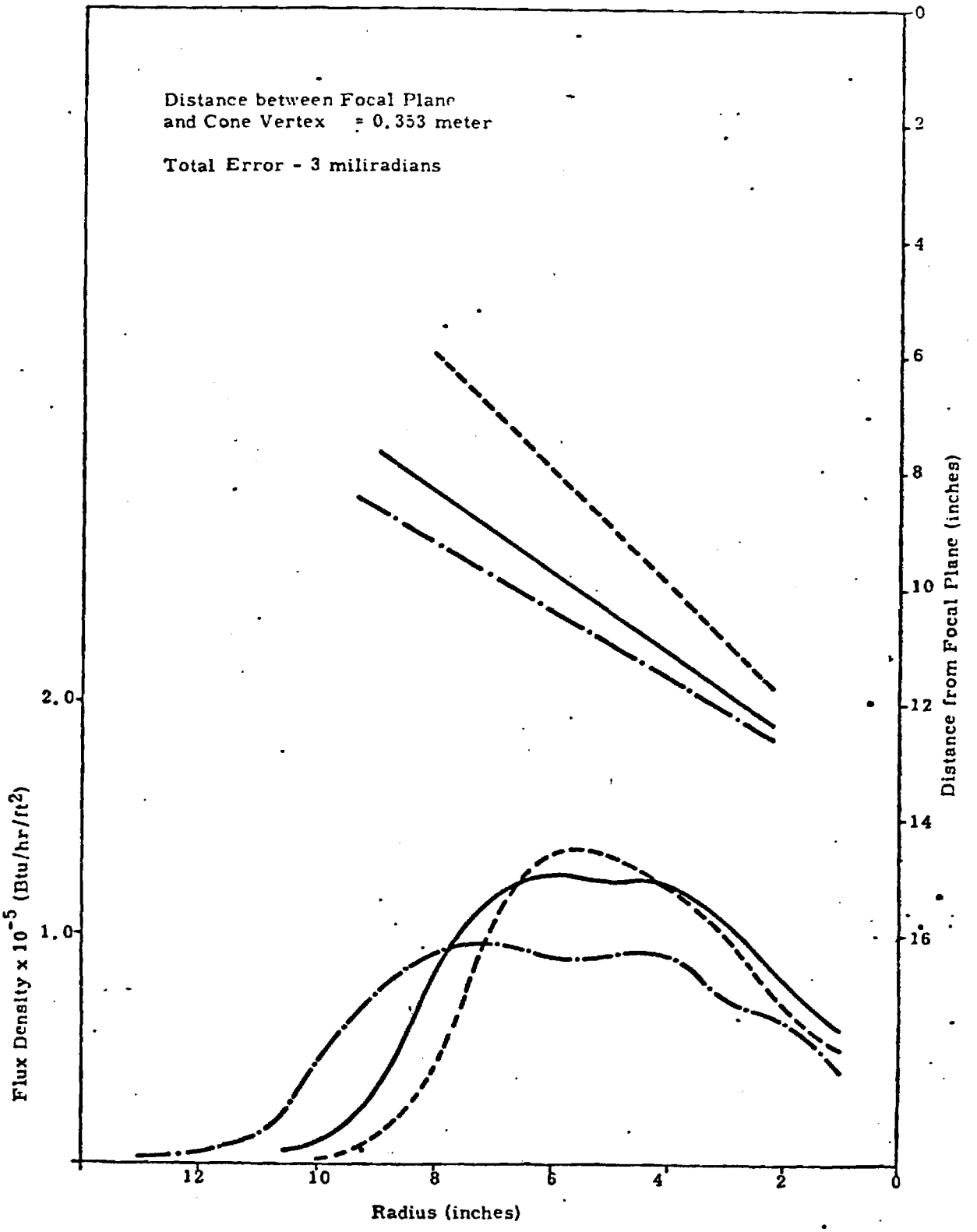

Figure 2-4. Receiver Cone Angle Effect

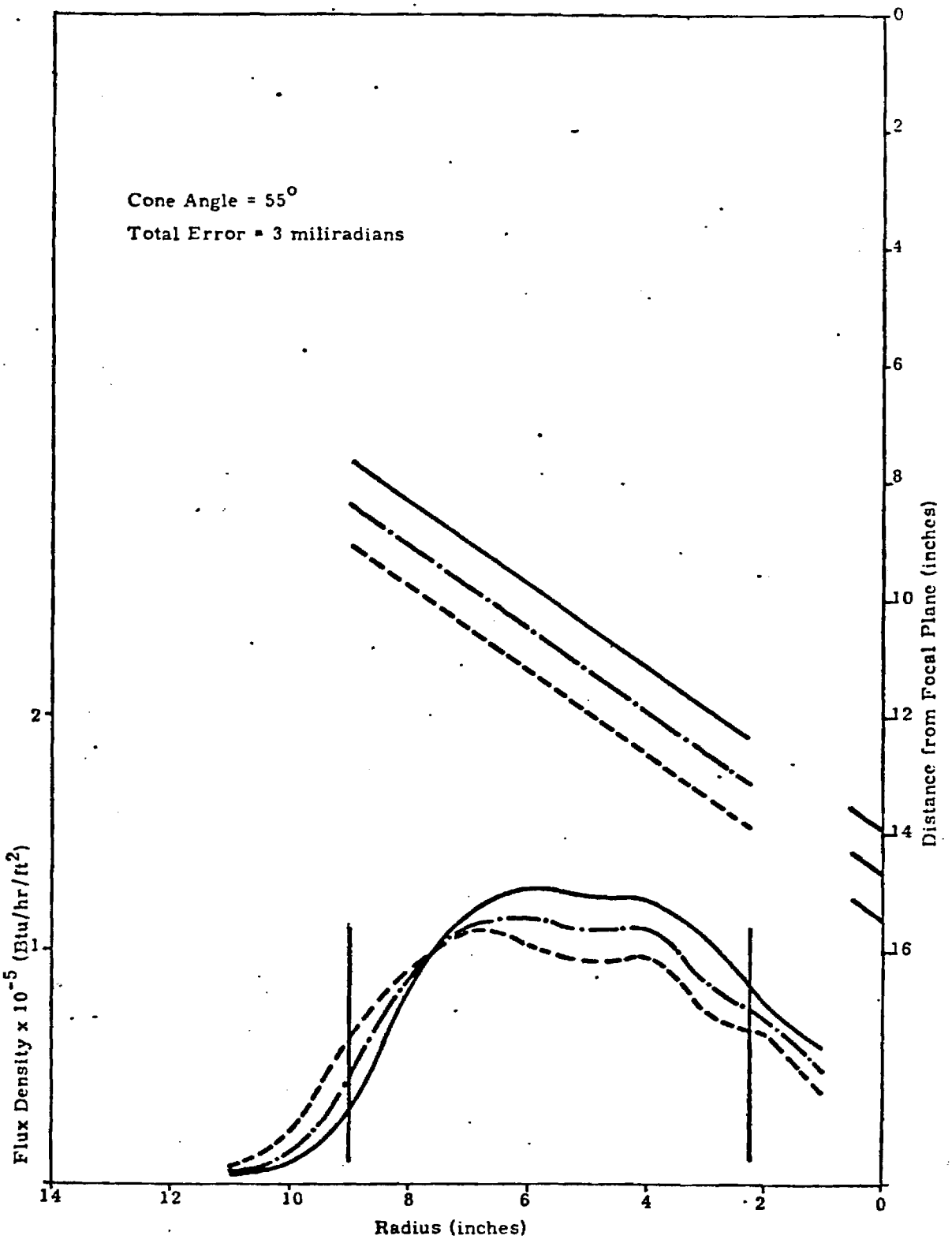

Figure 2-5. Receiver Cone Position Effect

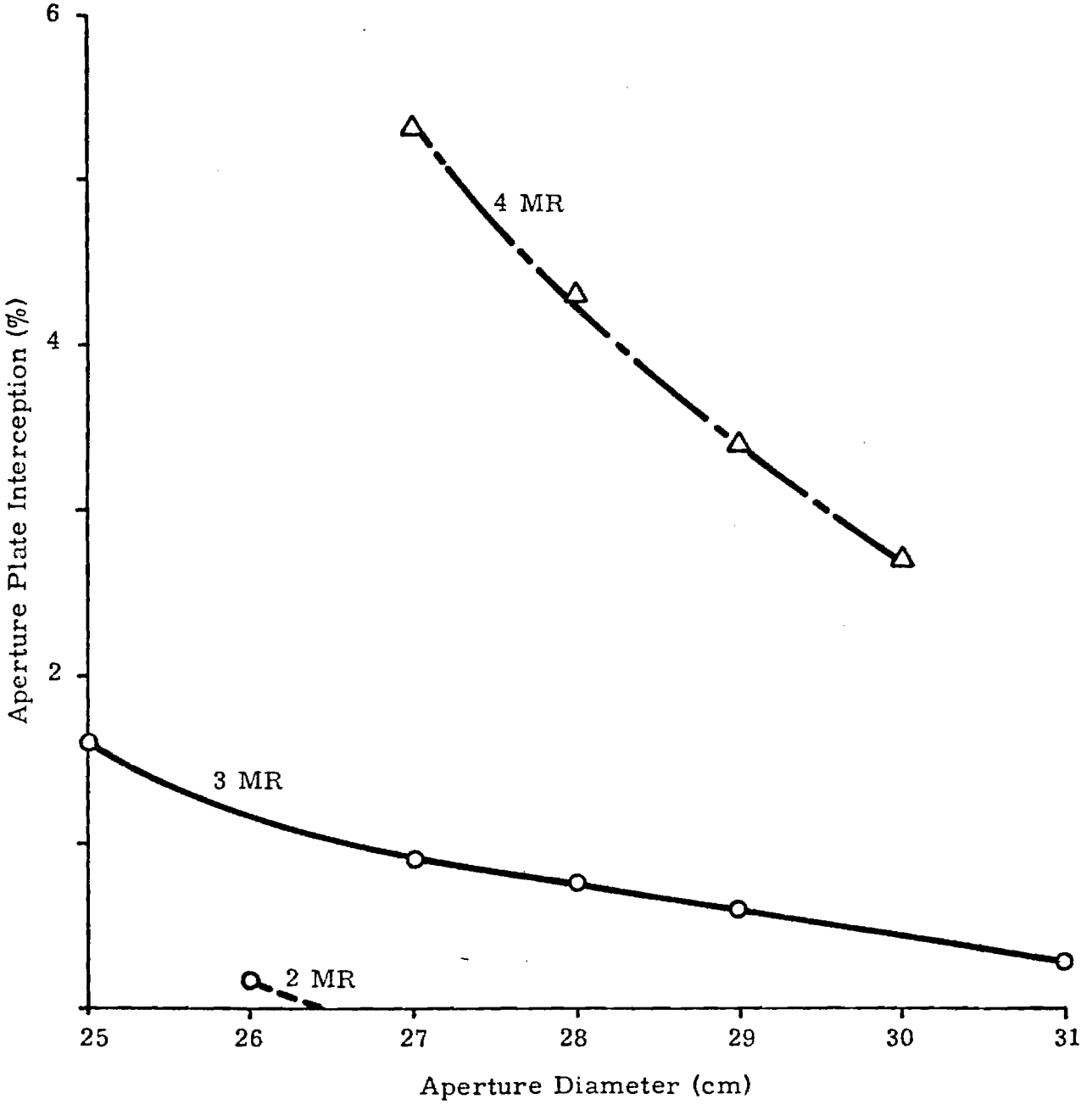

Figure 2-6. Effect of Slope Error on Aperture Plate Interception

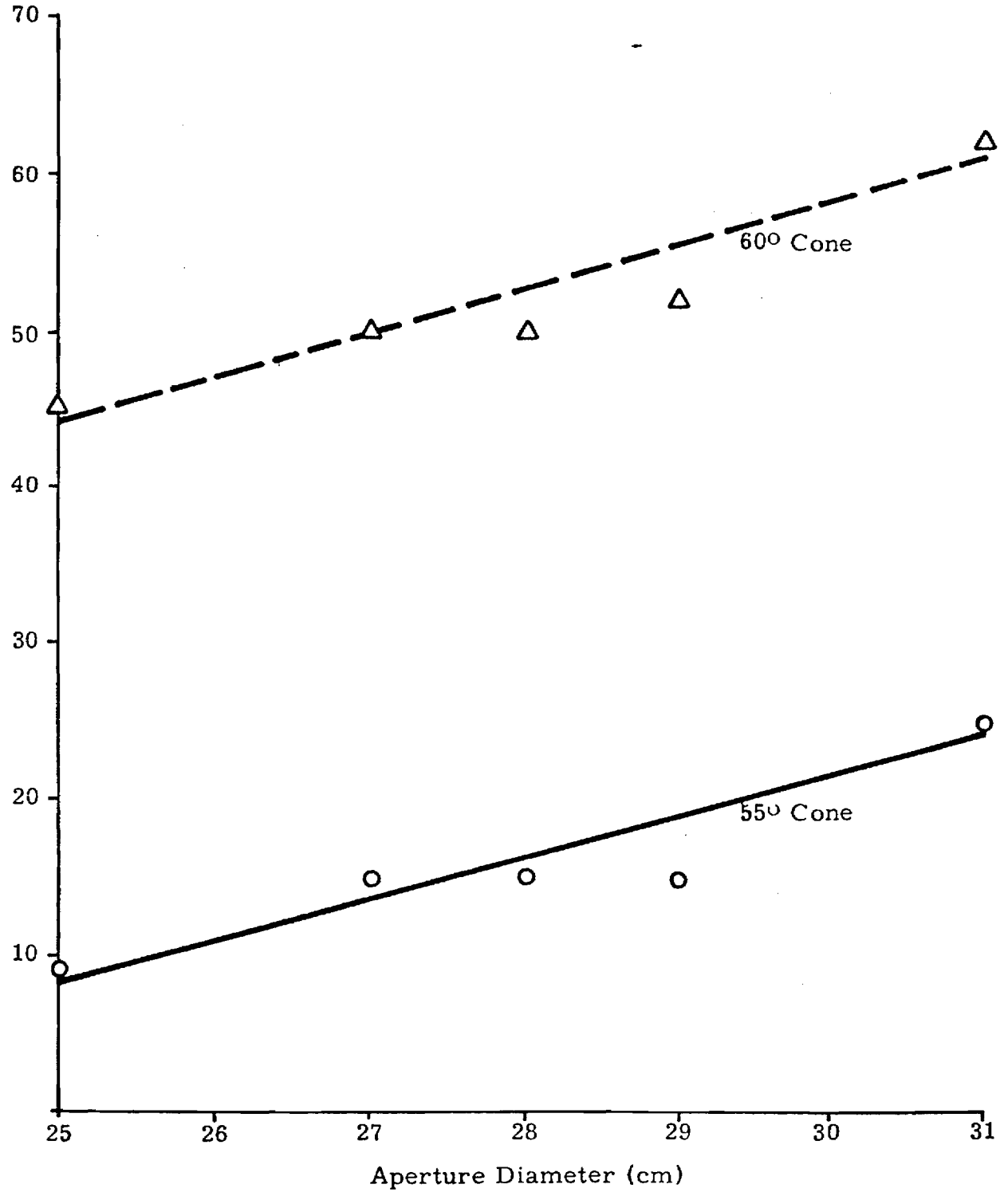

Figure 2-7. Effect of Aperture Size on Outer Cylinder Flux

Each time a different geometry was studied, the cycle consisted of performing an optical analysis to provide inputs to the thermal model. In this respect, it was extremely useful to keep the optical analysis simple. Well over 150 optical analysis runs were made. Results are consistent, and the few known shortcomings of the program do not detract from its utility.

2.5 THERMAL ANALYSIS

2.5.1 Description of Thermal Analysis Program

Thermal analysis was performed using a computer program known as MITAS, which is available on the Georgia Tech computing system. The MITAS system performs heat balances on a network of nodes and conductors to determine the temperatures of the nodes, either on a transient or steady state basis. The nodes in the MITAS network represent portions of the structure, presumably defined in such a way that there is little temperature variation over the volume which one chooses to define as a single node. In transient problems, it is necessary to specify a capacitance (mass x heat capacity) for each node. In steady state problems, it is more efficient to consider the nodes to have no capacitance. In either type of problem, one must specify conductances and initial temperatures.

Three types of conductances are used. The first is a thermal conduction term between two nodes in a solid material; it has the form kA/L, where k is the thermal conductivity of the material, A is the cross sectional area through which heat can flow between the nodes, and L is the path length for heat flow between the nodes. A conductance value must be generated between every node within a solid and its surrounding nodes. The second type of conductance is a convective term between a node on the surface of a solid and an adjacent fluid; it has the form hA, where h is the convective coefficient in the fluid and A is the cross sectional area between the solid node and the fluid. A convective conductance value must be generated

between every node in contact with fluid and the fluid itself. The third type of conductance is a radiative term between two nodes which can interchange heat by radiation; it has the form:

$$A_1 F_{12} \frac{1}{1/\epsilon_1 + 1/\epsilon_2 - I}$$

where is the Stefan-Boltzmann constant, A_1 is the area of the radiating node, F_{12} is the view factor from the radiating node to the receiving node, and ϵ_1 and ϵ_2 are the emissivities of the radiating and receiving surfaces. The user must specify a radiative conductance between all pairs of nodes which can "see" one another and have a high enough temperature for radiative transport to be significant. The user may also specify internal or external heat sources or sinks for specific nodes; in the present case, solar and combustion heat fluxes were external sources for certain surface nodes.

The user is required to specify an initial temperature for each node. In models containing a large number of nodes, this initial temperature estimate (in steady state problems, the term "initial" means before the iteration process begins) has a very pronounced effect on the number of iterations required to reach convergence. The user may specify a constant temperature on certain nodes; examples of this in the present problem are the constant helium working fluid temperature and the fixing of aperture temperatures at -460°F for radiation through the aperture to signify that energy passing out through the aperture is permanently lost.

The MITAS system contains two main parts--a pre-processor which collects all the user supplied input data and logic, and constructs

a FORTRAN program to solve the problem, and a library of subroutines, which the user calls as needed.

In steady state problems, which include all the cases run up to now on the Dish-Stirling Solar Receiver design, the initial temperatures are iterated until the temperature of each node has been readjusted to produce zero net heat flow into that node. When the maximum temperature change over an iteration is less than the prescribed value (user specified, we use 0.1 degree), the first convergence criterion is met. MITAS then evaluates two other criteria, system energy balance and energy balance for each node, and when these are met the iteration process stops. Steady state temperatures have then been determined within the network of nodes and conductances given. Since MITAS has no physical understanding of problem, it will achieve convergence of temperatures for whatever network of input data are supplied, including erroneous conductances if they are present. However, if it cannot find input data that are required, such as missing conductances, it will not run.

2.5.1 MITAS Models Constructed on This Program

The first MITAS models developed on this program concentrated on calculation of temperature distributions in the receiver walls, given external heat fluxes calculated by OPTIK, wall and fluid channel dimensions, and helium fluid temperatures. A typical three-dimensional node map for a section through a receiver panel is shown in Figure 2-8. For analytical convenience, the round helium passages were approximated as squares and the hA product for the square channel was taken to be the same value that would have existed for a

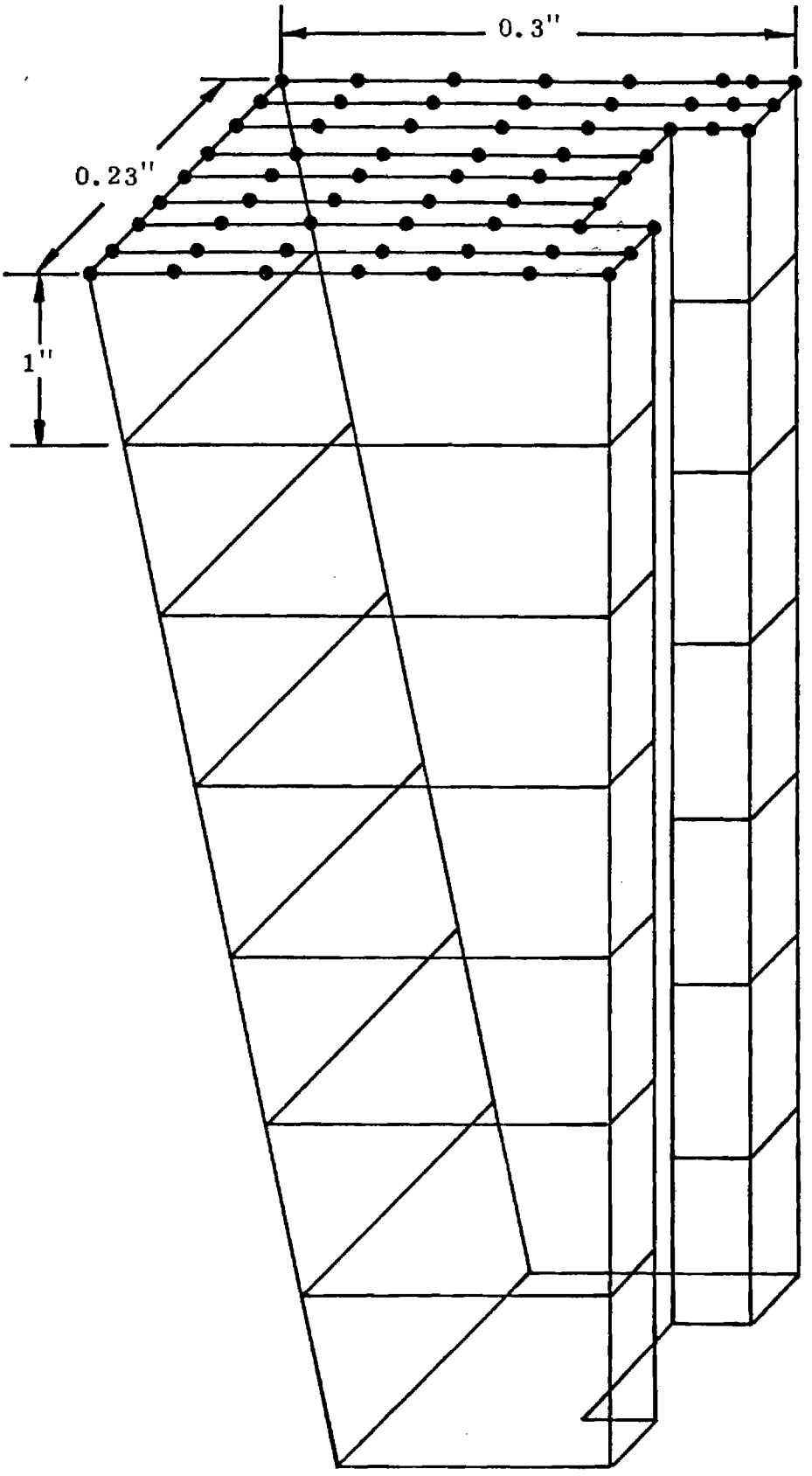

Figure 2-8. Mode Map for Three-Dimensional Section of Receiver Wall

round tube having the same cross sectional area. From symmetry considerations, the section of wall to be modeled was taken as half a cooling channel plus half the section between adjacent channels. Both two-and three-dimensional models were run during this period; approximately 20 runs were completed. The number of nodes in these solid models ranged from about 70 to more than 1,000.

The development of a MITAS model which accounted for radiant heat interchange among surface nodes was undertaken next. In order to perform this calculation, it is necessary to determine the view factors from each surface node to every other surface node. The view factor from a radiating node to a receiving node is defined as:

$$F_{12} = \frac{1}{\pi} \int \frac{\cos\phi_1 \cos \phi_2}{r^2} \, dA_2$$

where $_1$ and $_2$ are the angles between the normals to the radiating and receiving surfaces and the line connecting them, r is the distance from surface 1 to surface 2, and dA_2 is the area of the receiving surface. It can be shown that certain other relationships exist among view factors:

$$F_{12} + F_{13} + F_{14} + ... = 1 \qquad \text{and}$$

$$A_1F_{12} = A_2F_{21}$$

These are equivalent to stating that (1) the sum of the view factors from a radiating surface to all receiving surfaces is one and (2) the AF product from one to two is equal to the AF product from two to one. These relations are useful for checking calculations.

A program known as VUFAC was written to calculate view factors within a solar receiver cavity. The cavity interior was divided into rings around the cavity axis and each ring divided into 72 segments. Then the view factors from a segment on each ring to its own and all other rings were found and summed. The results from VUFAC were stored in a file in the computer and subsequently read into MITAS as input data. The data from each VUFAC run were also printed so that the checks described above could be applied by inspection.

When the MITAS runs for the cavity with radiant heat transport were made, it became apparent that the number of nodes in the wall conduction model should be reduced because computing time had become prohibitive. (The number of radiation conductors is $n(n-1)/2$, where n is the number of surface and aperture nodes; when the total number of conductors is more than 1,000, computing time becomes excessive.) Thus, two separate MITAS models were used: a 16 node model (one for center plug, six for active receiver surface, one for cylindrical wall, one for aperture plate, four for helium passage walls, one for helium fluid, two for aperture) and a 343 node model which included 12 planes in the active receiver wall with 28 nodes per plane. This latter model was needed to obtain temperature distributions within the metal receiver wall. About nine MITAS runs were made with these models to check various combinations of geometry and materials. A typical node map for a 16-node MITAS model is shown in Figure 2-9.

Next, an investigation of cavity heat losses by convection to the atmosphere was undertaken. An exact solution to this problem has not yet been achieved because it is not possible to specify the velocities

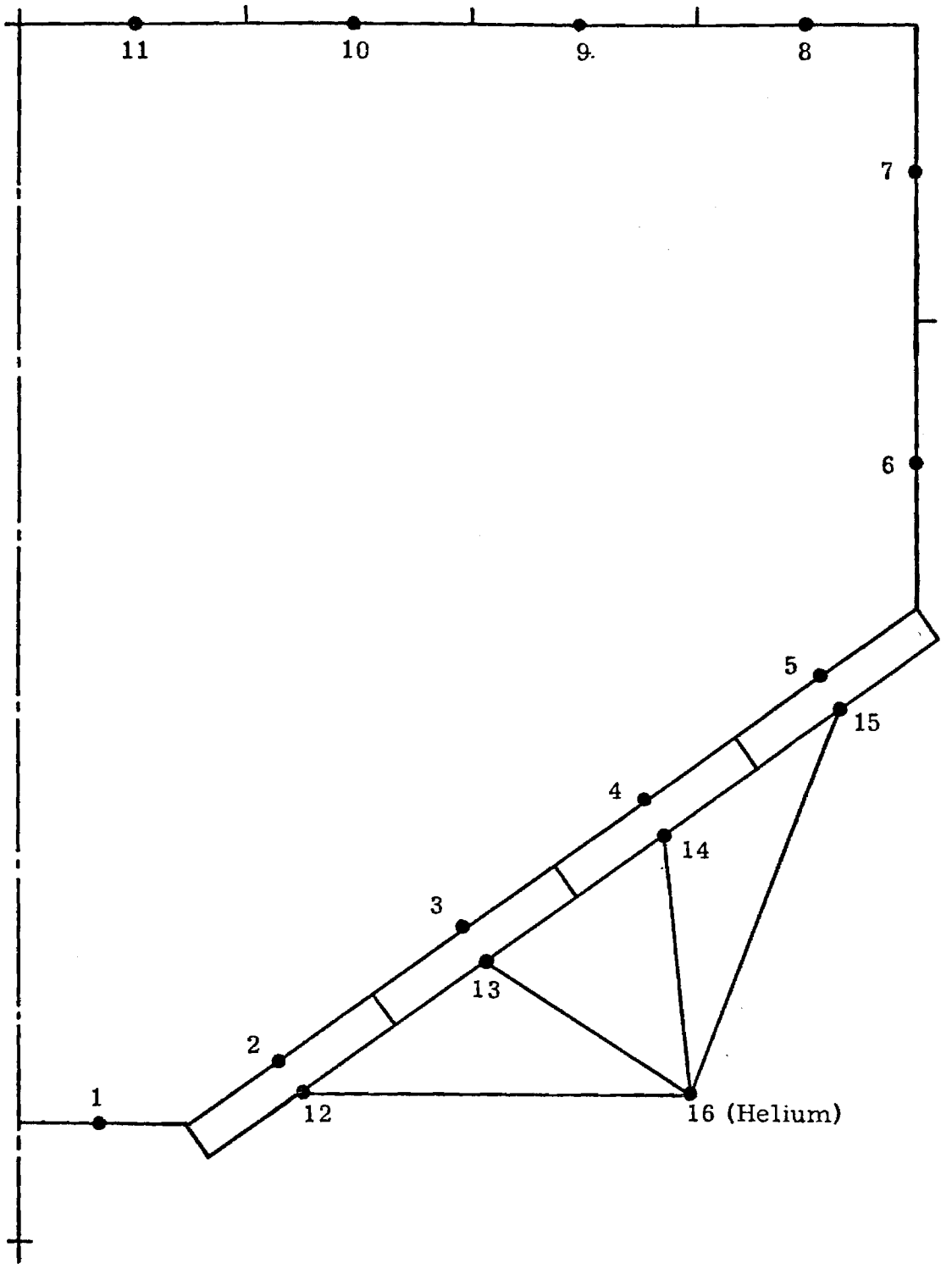

Figure 2-9. Mode Map for 16-Node MITAS Model

and flow patterns for air within the cavity. However, the approach was to establish boundaries for heat loss magnitudes in order to determine their importance. The MITAS models were changed to include a boundary node representing the ambient air; the air temperature was set at 200°F which is hardly more than a guess. Free convection h values of 1, 5, and 10 Btu/hr ft^2 °F were assumed to bracket the range of values considered reasonable. Only the value of h equal to 1 gave heat loss values similar to experimental results on other cavities. MITAS contains a subroutine to calculate free convection h values which gives results also in the order of 1.

An additional short study of losses by free convection was conducted to acquire independent estimates of the convective coefficients and air temperatures. It appeared that when wind velocities across the aperture were about three miles per hour or greater, the heat transfer mechanism could change from free convection to laminar forced convection on the cylindrical cavity walls. Using standard correlations, the convective coefficients were estimated to range from about 1.2 to 2.5 Btu/hr ft^2 °F for free-stream air temperatures of 100 to 300°F. Air temperatures in the range of 250 to 300°F were also estimated at distances of 0.275 inch from the vertical wall. These findings tend to support the values of parameters used in the MITAS analyses, although the area of convective losses is still inadequatly understood at the present time.

After the MITAS analyses had evolved to the present stage of sophistication, accounting for radiant heat transport within the cavity, conduction through the receiver wall to the fluid channels,

convection to the helium, input heat fluxes from combustion and solar radiation, and convective losses, a variety of runs were made to support parametric design analyses. These included:

1. 18 runs on brazed Inconel receiver with 9-inch cavity radius.
2. 14 runs on brazed Inconel receiver with 11-inch cavity radius.
3. 18 runs on copper-clad Inconel receiver with 11-inch radius.
4. 1 run on copper-clad Inconel receiver with thicker copper at large receiver radii.
5. 2 runs on copper-clad Inconel receiver with newly specified parameters for JPL Test Bed Concentrator.
6. 3 runs on copper-clad Inconel receiver with helium temperatures of 1200, 1300, and 1400°F.

The results of these MITAS analyses were used to identify optimized design configurations for the Dish-Stirling Solar Receiver. The MITAS system provides a powerful design tool for studies of this kind since it is capable of analyzing a complex geometry and accounting for many different thermal effects. The intial setup for MITAS runs is a lengthy procedure, however. The user must identify the node points, specify all conduction, convection and radiation heat flow paths, specify heat inputs at each node, and specify initial temperatures. Much of this work is done by computing logic rather than by individual data statements, but several days are needed to begin operation of a new model.

Table 2-3
Configuration - Inconel 617 Brazed
Cone Angle 55°

Aperture Error	25 3	27 3	28 3	29 3	31 3	28 2	28 4
T_1	2558	2550	2546	2541	2534	2378	2556
T_2	1718	1716.1	1715	1714	1712	1714	1713
T_3	1813	1811.6	1811	1810	1808	1806	1812
T_4	1778	1776.5	1775	1775	1772	1792	1757
T_5	1795	1792	1790	1788	1784	1790	1790
T_6	2055	2047	2040	2033	2020	1943	2172
T_7	1979	1977	1968	1959	1941	1859	2097
T_8	1816	1799.7	1788	1777	1760	1707	1895
T_9	1862	1834	1823	1810	1787	1734	1987
$Q_{Hel/72}$	2953.6	2952.6	2940.1	2932.2	2913.9	2995.5	2791.5
$Q_{Rad/72}$	206.5	238.2	253.6	269.5	302.4	230.7	282.8
$Q_{Conv/72}$	256.3	252.3	249.9	247.5	242.9	237.7	267.3
$Q_{Front\ Plate/72}$	52	28	24	19	9	0	138
Rec.Eff.	.85157	.8504	.8479	.8455	.8402	.8648	.8022
$Q_{Total\ Lost\ Btu/Hr}$	37065.6	37404	37980	38592	39910	33725	49543.2

Table 2-4
Configuration -Inconel 617 Brazed
Cone Angle 60°

Aperture Error	25 3	27 3	28 3	29 3	31 3	28 2	28 4
T_1	2593	2581.6	2576	2572	2561	2397.6	2543
T_2	1721	1718	1717	1716	1714	1716	1715
T_3	1806	1803	1801	1800	1798	1796	1806
T_4	1772	1769	1768	1767	1764	1774	1756
T_5	1835	1828	1825	1823	1819	1836	1814
T_6	2272	2258	2250	2243	2239	2155	2325
T_7	2182	2163	2153	2143	2124	2033	2264
T_8	1933	1909	1896	1886	1864	1805	1979
T_9	1965	1931	1919	1907	1882	1823.7	2059
$Q_{Hel/72}$	2912.8	2892.2	2877.7	2868.4	2845	2928.9	2717
$Q_{Rad/72}$	248.3	282.9	300.7	319.1	356.8	268.9	327.7
$Q_{Conv/72}$	287.2	281.7	279.0	276.4	271.1	265.0	293.2
$Q_{Front\ Plate/72}$	52	28	24	19	9	0	138
Rec.Eff.	.8321	.8300	.8266	.8235	.8171	.8458	.7816
$Q_{Total\ Lost}$ Btu/Hr	42300	42667	43466	44244	45856	38441	54641

Table 2-5
Configuration - Inconel 617 Tubes Imbedded in Copper
Cone Angle 55°

Aperture Error	25 3	27 3	28 3	29 3	31 3	28 2	28 4
T_1	2306	2301	2299	2296	2293	2154	2299
T_2	1620	1619	1619	1619	1618	1618	1616
T_3	1650	1650	1650	1650	1650	1650	1648
T_4	1608	1608	1607	1607	1607	1614	1601
T_5	1626	1625	1624	1623	1622	1625	1629
T_6	1683	1679	1677	1674	1671	1665	1717
T_7	1685	1678	1675	1671	1666	1648	1730
T_8	1652	1643	1638	1633	1628	1608	1698
T_9	1664	1635	1628	1618	1602	1578	1775
$Q_{Hel/96}$	2278.0	2282.7	2278.6	2279.3	2270.3	2344.2	2164.5
$Q_{Rad/96}$	108.15	125.2	134.2	143.3	162.9	124.4	141.66
$Q_{Conv/96}$	166.7	164.2	163.1	161.87	159.7	159.7	171.3
$Q_{Front\ Plate/96}$	52	28	24	19	9	0	138
Rec.Eff.	.8784	.8816	.8802	.8790	.8760	.8936	.8325
$Q_{Total\ Lost}$ Btu/Hr	30298	29419	29780	30046.6	30735	26793.6	41802

Table 2-6
Configuration - Inconel 617 Tubes Imbedded in Copper
Cone Angle 60°

Aperture Error	25 3	27 3	28 3	29 3	31 3	28 2	28 4
T_1	2212	2207	2205	2203	2199	2068	2166
T_2	1609	1608	1608	1608	1607	1607	1605
T_3	1630	1630	1629	1629	1629	1629	1628
T_4	1598	1597	1597	1597	1596	1600	1593
T_5	1636	1633	1632	1631	1630	1631	1633
T_6	1708	1703	1701	1699	1696	1677	1724
T_7	1717	1710	1706	1703	1698	1667	1747
T_8	1686	1677	1672	1669	1662	1630	1718
T_9	1683	1654	1646	1637	1621	1586	1784
$Q_{Hel/96}$	2288.6	2285.4	2278.6	2275.7	2267.2	2297.3	2153.8
$Q_{Rad/96}$	113.9	131.6	141.0	150.8	171.2	133.6	
$Q_{Conv/96}$	179.9	177.3	176.1	174.9	172.6	171.1	
$Q_{Front\ Plate/96}$	52	28	24	19	9	0	138
Rec.Eff.	.872	.875	.873	.8719	.869	.886	.826
$Q_{Total\ Lost}$ Btu/Hr	32198	31373	31763	32098	32852	28373	43631

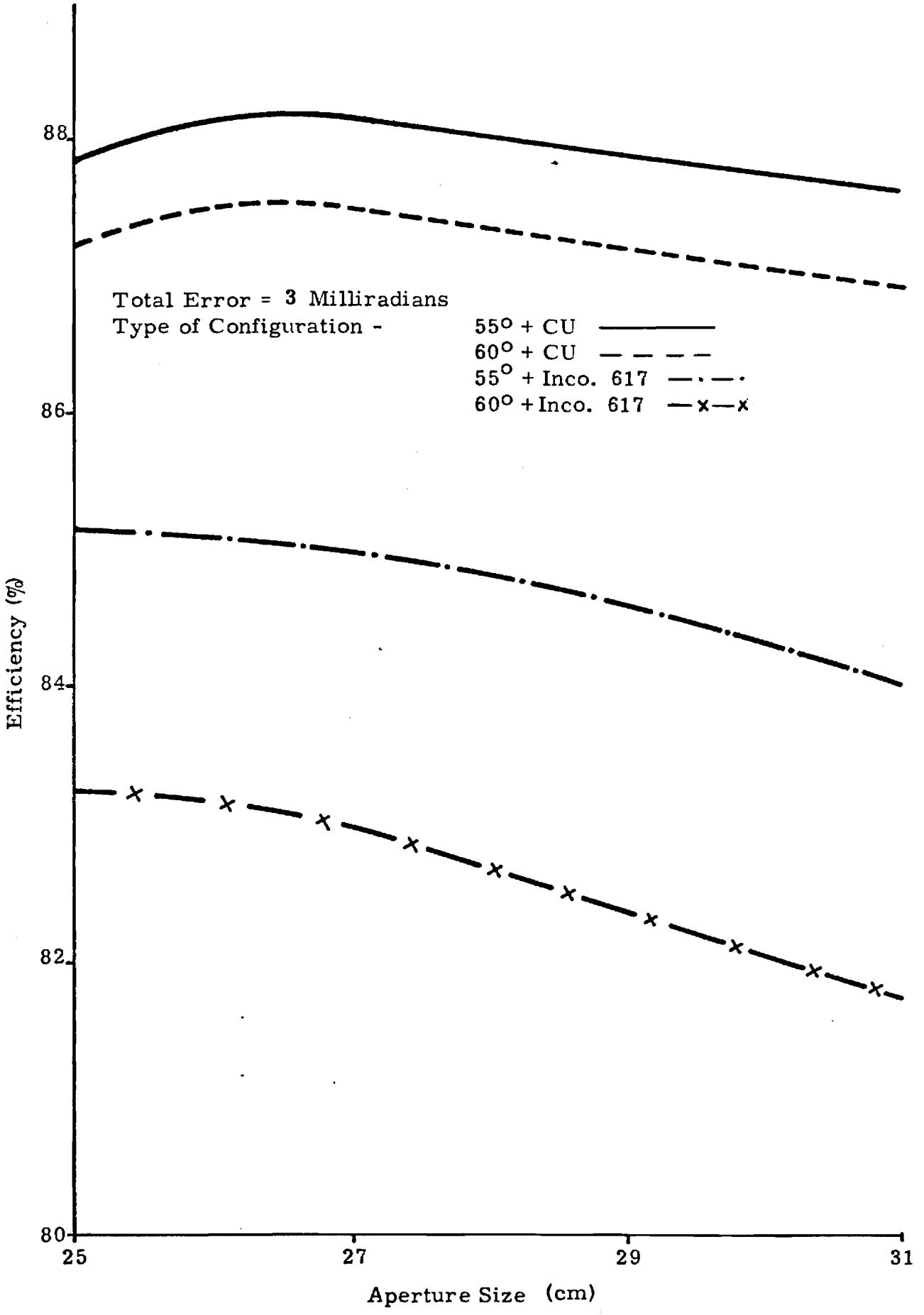

Figure 2-10. Aperture Size Effect for Various Configurations

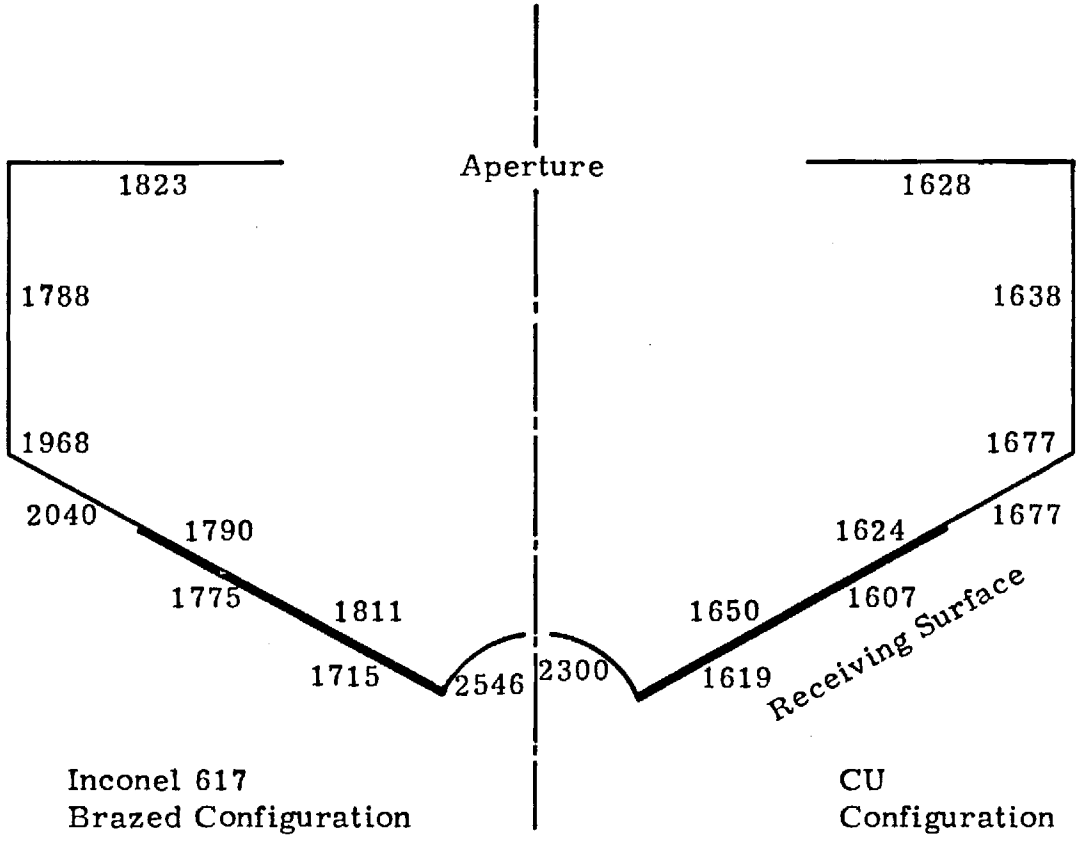

Figure 2-11. Typical Temperature Distribution Within Cone (55°, 3 MR)

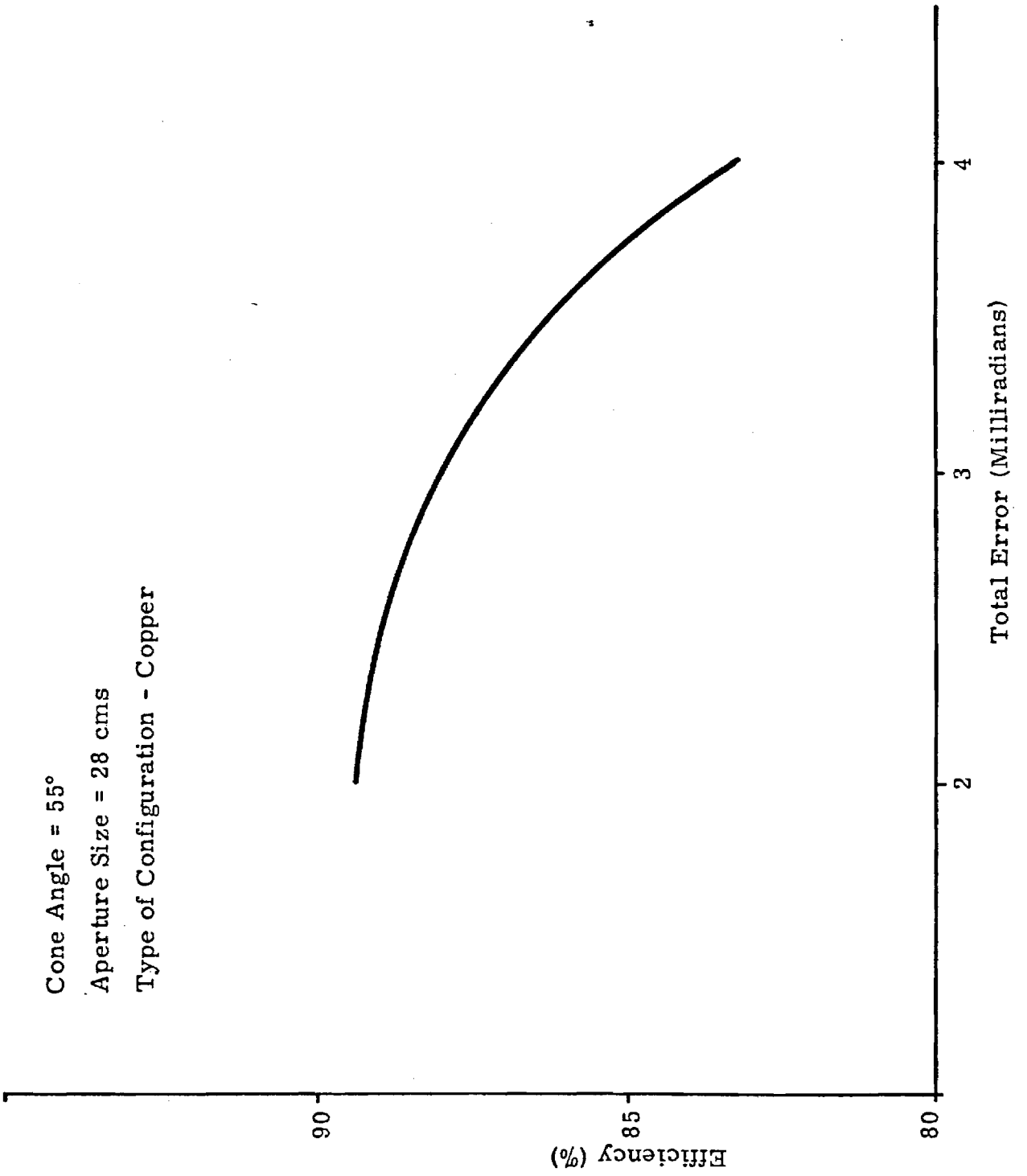

Figure 2-12. Concentrator Total Error Effect

Table 2-7
Effect of Adding Copper

At the Diameter where Flow Passage Turns Around

Cone Angle = 55°

Aperture Size = 28 C.M.S.

Total Error = 3 Milirandians

Configuration = Copper with Inconel 617 tubes

Case	Uniform Copper	Copper Added
T_1	2299	2295
T_2	1619	1616
T^3	1650	1647
T_4	1607	1608
T_5	1624	1618
T_6*	1677	1658
T_7*	1675	1653
T_8	1638	1623
T_9	1628	1615
Receiver Efficiency*	.881	.887

*Improvements

Table 2-8
Effect of Flow Passage Length

Configuration - Copper with Inconel 617 Tubes
Cone Angle - 55°
Aperture Size - 28 C.M.S.
3 Miradians - Total Error

Length (Inches)	18	17	16	15	14
Error	3	3	3	3	3
T_1	2286	2288.6	2299	2319	2400
T_2	1617	1618	1619	1622	1636
T_3	1647	1648	1650	1655	1683
T_4	1603	1601	1607	1622	1718
T_5	1575	1590	1624	1742	2265
T_6	1556	1580	1677	1829	2237
T_7	1573	1593	1675	1805	2163
T_8	1549	1567	1638	1755	2084
T_9	1555	1570	1628	1730	2059
Q_{Hel}	2384.3	2379	2278.6	2322.9	2175.5
Rec. Eff.	.890	.888	.8802	.867	.812

Figure 2-16
EFFECT OF FLOW PASSAGE LENGTH

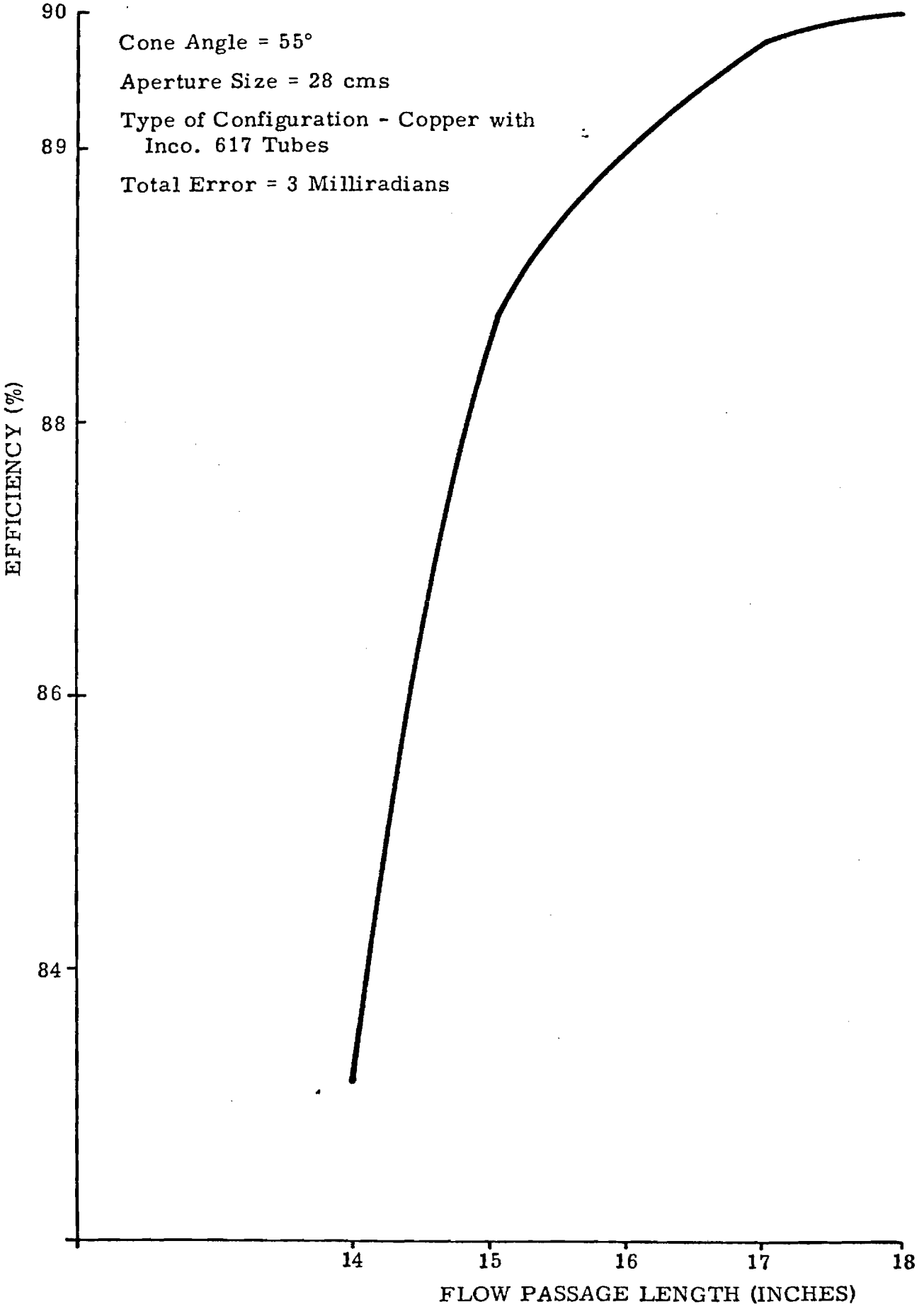

Table 2-9
Effect of Helium Temperature

Cone Angle = 55°

Aperture Size = 28 C.M.S.

Total Error = 3 Miliradians

Configuration = Copper with Inconel 671 tubes

	1300°	1500°
T_1	2176	2299
T_2	1422	1619
T_3	1452	1650
T_4	1409	1607
T_5	1429	1624
T_6	1492	1677
T_7	1500	1675
T_8	1469	1638
T_9	1452	1628

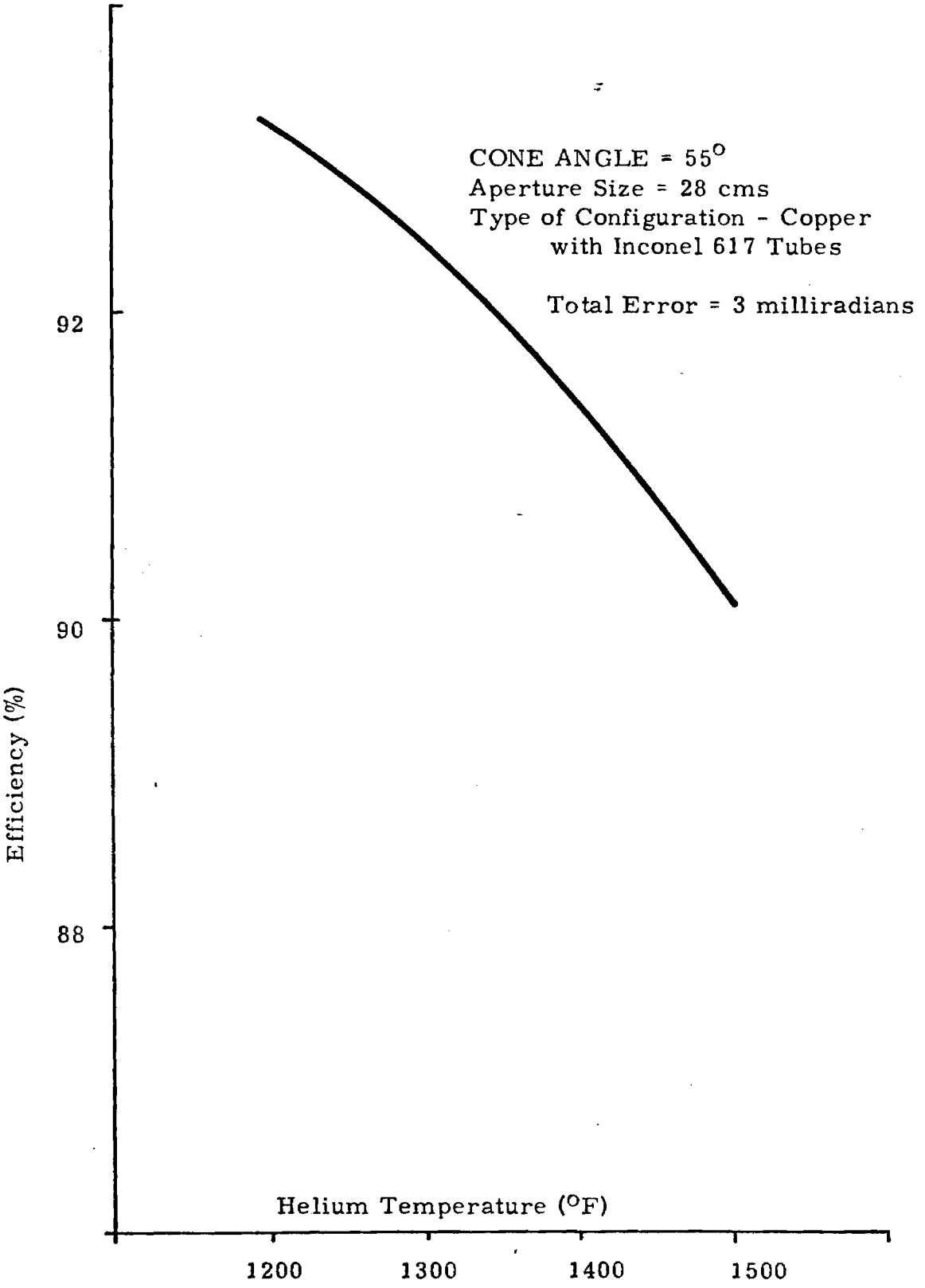

Figure 2-14. Effect of Helium Temperature

Table 2-10
Selected Configuration

Configuration	Copper with Inco. 617 Tubes
Cone Angle	55°
Cone Vertex from Focal Plane	0.353 meter
Flow Passage Length	17 inches
Helium Temperature	1300° - 1500°F
Aperture Size	28 C.M.S
Special Change	Add Copper where Flow Passage Turns Around

87.6% Receiver Efficiency 88%

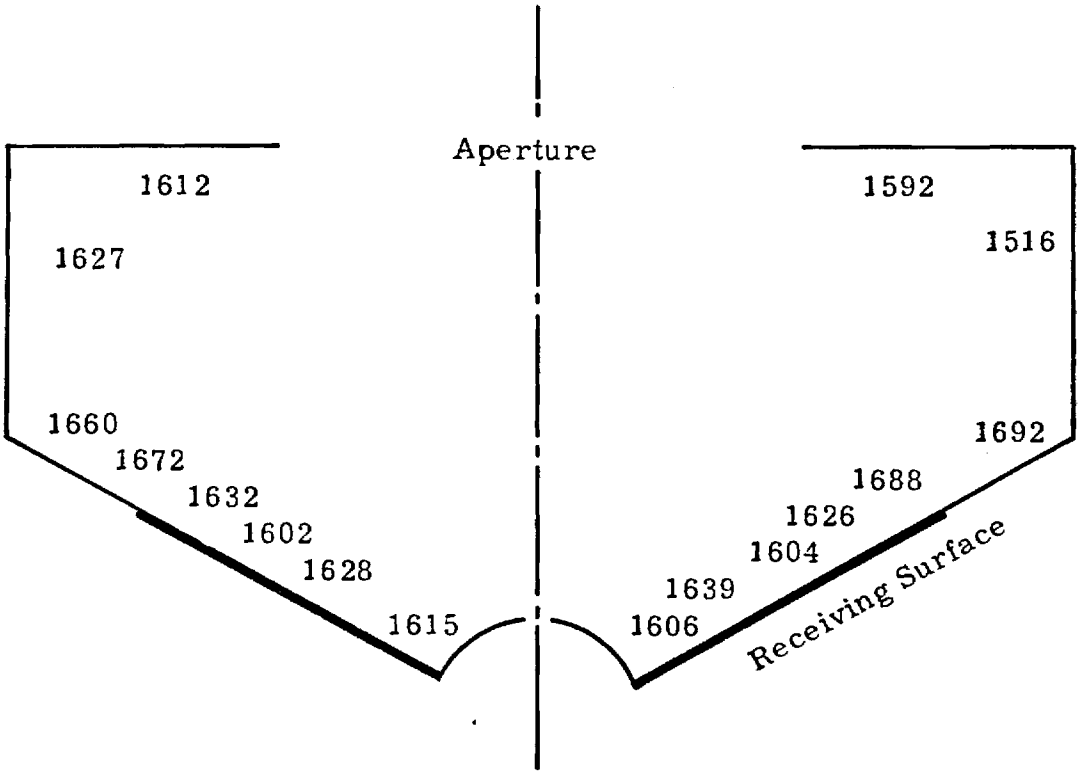

Test Bed Concentrator Advanced Concentrator

Figure 2-15. Typical Temperature (^{o}F) Distribution Within Cone

FINAL REPORT

PROJECT A-2348

DISH STIRLING SOLAR RECEIVER DESIGN REPORT

By

S. H. Bomar, Jr.
R. D. Chelf
T. B. Elfe
J. N. Harris
J. H. Murphy

September 1979

Prepared for

Fairchild Stratos Division
Manhattan Beach, CA 90266

Engineering Experiment Station
Georgia Institute of Technology
Atlanta, Georgia 30332

SECTION 2.0

OPTICAL AND THERMAL ANALYSIS

2.1 OPTICAL ANALYSIS

2.1.1 Sun Model Verification

A series of optical analysis runs was made to determine whether a significant error is being introduced by using solar rays emanating from the center of a ring 12 to 16 feet from sun center to represent the outermost sun rays. The optical analysis program was modified so that the third ring (formerly the 12 to 16-foot ring) extended from 12 to 15.5 feet. A fourth ring (15.5 to 16 feet) was added, and any ill effects of the previous approximation were magnified by considering that rays from the fourth ring originated at 16 feet.

Runs were made on the focal plane and on the receiver surface for 2, 3, and 4 milliradian slope errors, using the Advanced Concentrator parameters. The results are summarized in Tables 2-I and 2-II. Despite minor differences, it appears that the original sun model is sufficiently accurate to be used for the remainder of the design work.

2.1.2 Test Bed Concentrator Model

The optical analysis program was modified to model the Test Bed Concentrator. In this model, it was assumed that the

Table 2-1. Flux Density (kw/m^2) on Focal Plane for 14' and 16' Sun Models

Sun Extremity (radius, in.)	= 2mRAd		= 3mRad		= 4mRad	
	14'	16'	14'	16'	14'	16'
0	11180	11036	6433	6327	4187	3783
1	7616	7632	4923	4894	3296	3369
2	2741	2749	2719	2742	2239	2242
3	556	539	1117	1127	1263	1263
4	61	68	356	346	606	601
5			74	82	241	242
6			15	10	85	84
7					20	21

Table 2-2. Flux Density (kW/m^2) on 55# Cone 0.353 m Focal Plane-Vertex Spacing for 14' and 16' Sun Models

Sun Extremity (radius, in.)	= 2mRad		= 3mRad		= 4mRad	
	14'	16'	14'	16'	14'	16'
1	126	130	187	182	234	229
2	258	253	247	241	243	231
3	336	327	332	318	320	299
4	382	381	383	375	389	377
5	378	373	392	385	394	385
6	424	427	395	396	362	364
7	417	414	364	354	304	296
8	259	260	254	265	255	260
9	71	76	95	105	125	138
10	18	20	29	31	43	48
11	3		14	14	18	20
12					9	10

normal at the center of each facet would coincide with the normal of a paraboloid having a focal length of 6.6 meters, and an f/D ratio of 0.6. Systematic slope errors, which arise because the facets are spherical, rather than paraboloidal, were calculated for points on the edge of each facet. Systematic errors for other points on a facet were derived by parbolic interpolation. The normal at each point on the concentrator was then assigned a slope error which was the vector sum of the systematic error and a randomly directed error, having a standard deviation of 1 milliradian.

Since the Georgia Tech optical analysis program treats points along a plane curve on the concentrator and assumes a symmetric flux pattern, it was decided that points along three "lines," horizontal, vertical, and diagonal, should be averaged to arrive at a more realistic flux pattern. This is essentially similar to the logic which would have been used, had the analysis program been expanded to a true 3-dimensional program, which time did not permit. Since the Test Bed Concentrator provides considerably more flux than the Advanced Concentrator, the model was set up to analyze a masked Test Bed Concentrator. This was done by modifying the weighting function which weighs rays according to their points of origin on the concentrator.

Figure 2-1 shows the masked Test Bed Concentrator flux pattern on the receiver surface. It also shows the Advanced Concentrator flux pattern for reference.

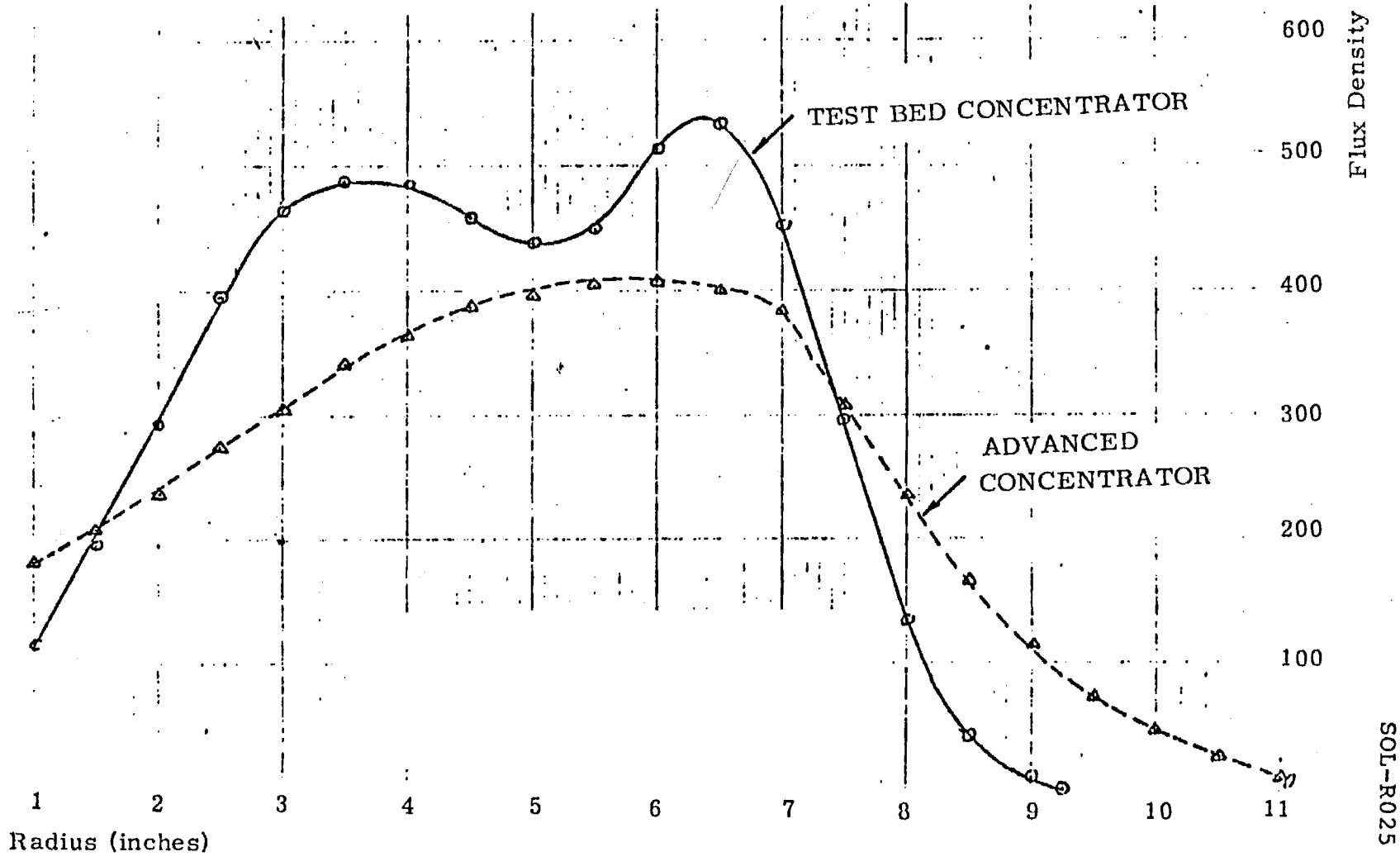

Figure 2-1. Flux Pattern From
Test Bed Concentrator

2.2 THERMAL ANALYSIS

Several improvements were made to the thermal analysis model. The need for some of these improvements was apparent before PDR, but time did not permit them to be made at that time. These improvements included taking into account the different values of reflectivity and emissivity of the various surfaces in the receiver and devising a technique for converting the rectangular tube model to a circular one.

2.2.1 Reflectivity Considerations

The pre-PDR thermal model implicitly assumed zero reflectivity for all receiver surfaces. A short computer program was written to read solar and combustor heat input and reflectivity for each node from a data file. For a given node, the absorbed flux is accumulated, reflected flux is distributed to the other nodes, according to the same view factors which are used to calculate radiation conductors, and reflected flux which arrives at aperture nodes is permanently lost. This absorption and re-reflection process is continued until the flux which is still "bouncing around" is less than 0.1 percent of the original incident flux. Modified heat input for each node is written to a file, which is later edited into the MITAS input file.

Several important features are seen in runs made with the improved model. Approximately 2.5 percent of the incident flux is reflected from the aperture plate and from internal surfaces

through the aperture. The aperture plate and center plug do not run as hot as the pre-PDR runs indicated. Heat into the receiver is redistributed, and efficiency and temperatures can be manipulated somewhat by blackening or whitening certain surfaces.

2.2.2 Emissivity Considerations

The modification to include individual emissivities for the various nodes was straightforward. The radiation conductances, which are generated by an auxiliary computer program, are modified by the emissivities of the transmitting and receiving nodes. In the process of making this modification, it was found that in concentrating on proper modeling of the cavity interior, the radiation from the aperture plate into space had been overlooked. This was corrected, resulting in a slight loss of efficiency.

2.2.3 Improved Model of Tubing

In the pre-PDR models, it was difficult to calculate gradients in the Inconel tubing for two reasons. First, the model treated the tubing as rectangular, and second, the circumferential spacing between all nodes was proportional to the cone circumference. The latter had the effect of having too few nodes in the outer area of the cone.

The improved model uses an octagonal tube. It also maintains a constant node spacing in the tube area, letting the spacing between nodes in the copper expand with the geometry of the

cone. In addition, the definition is further improved by taking temperatures in the copper at a constant distance from the tube center and using these temperatures as boundary node temperatures in a series of two-dimensional radial models. Since the effects of radiation and convection are "built into" the copper boundary temperatures, these two-dimensional models must only treat conduction.

2.2.4 Isothermal Maps

The temperatures derived from the combined large model - two dimensional radial model runs were used to make the isothermal plots shown in Figures 2-2 (a-g) and 2-3 (a-g). The isotherms in Figure 2-2 (a-g) are for a helium temperature of 1200°F, while those in Figure 2-3 (a-g) are for a temperature of 1500°F.

2.2.5 Efficiency and Temperature

A number of small model (17 node) runs were made to ascertain the effect of various parameters on receiver efficiency and temperature. In general, lower helium temperature results in higher receiver efficiency. It should also be noted that the convection losses are expected to be much lower than predicted by the MITAS convection model. Therefore, the values presented should not be taken as absolute. For this reason, heat into helium is used as a comparison standard. Flux incident on the receiver was 67 kW in in all cases. Table 2-III shows the result of these runs.

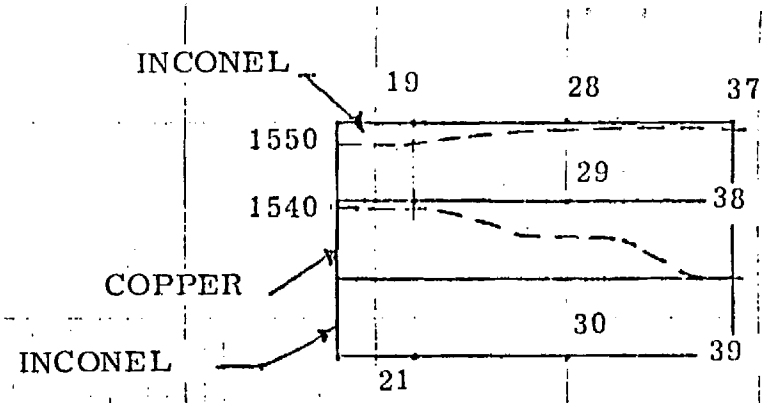

Cone Radius - 2.38"

Figure 2-2a. Plane 1

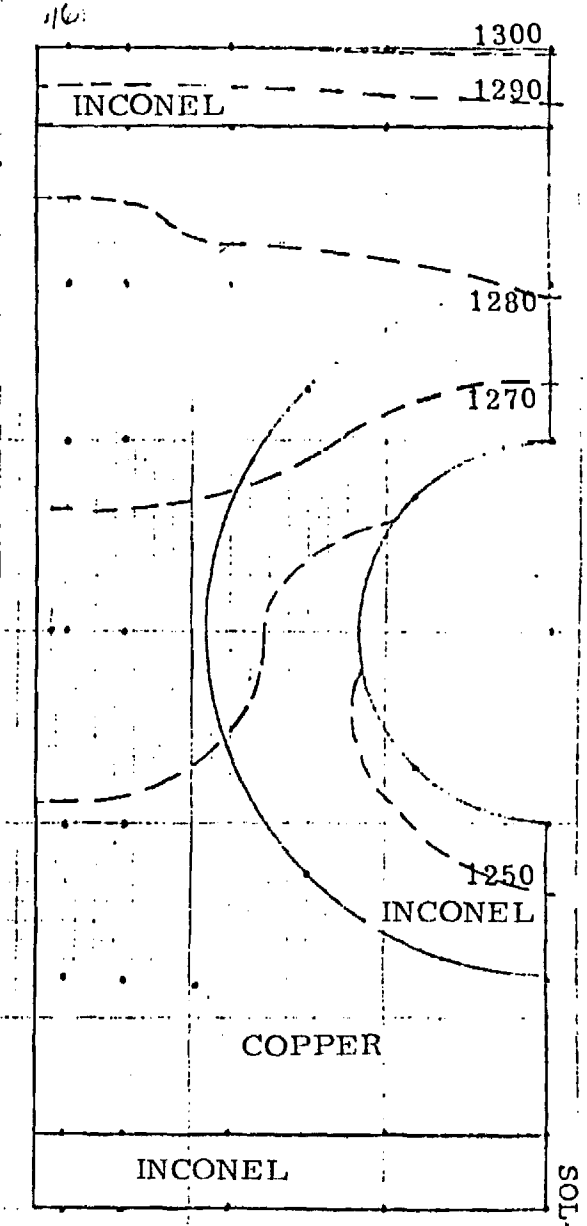

Cone Radius = 3.06"

Figure 2-2b, Plane 2

SOL-R025

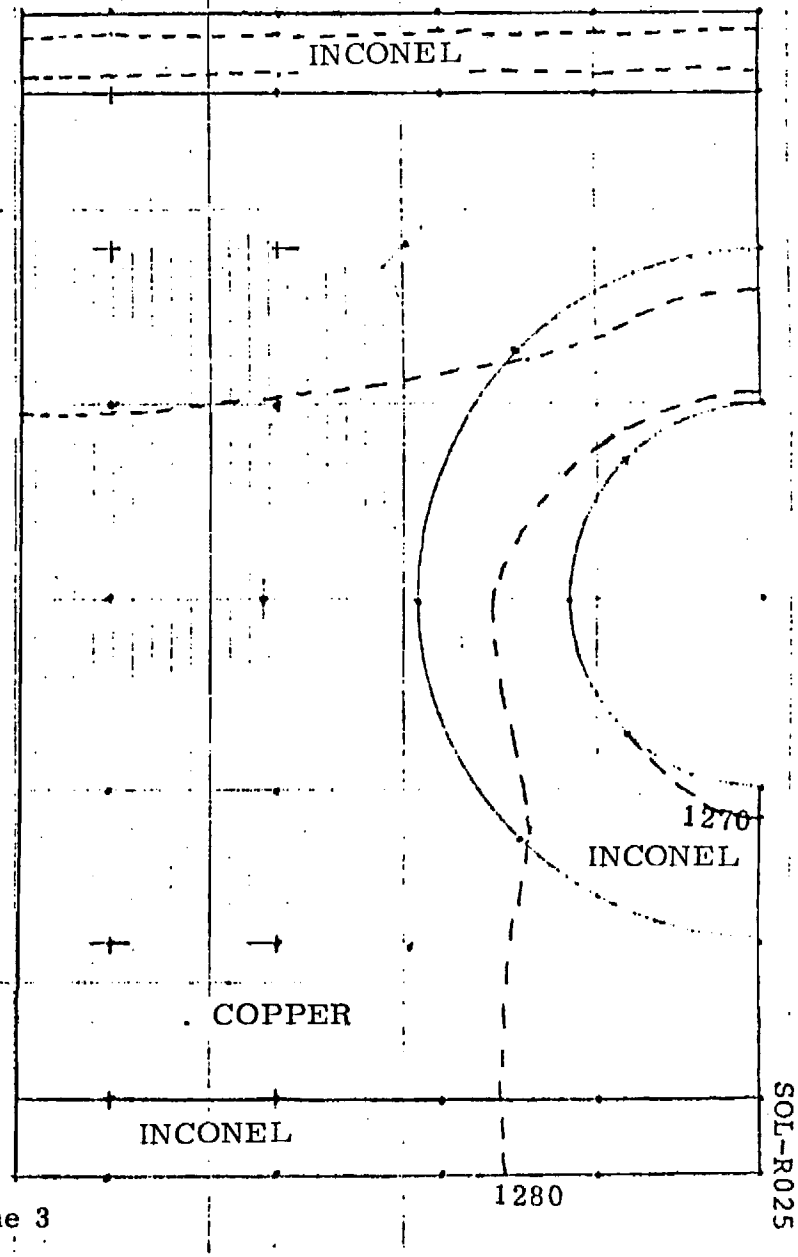

Cone Radius = 4.36"

Figure 2-2c. Plane 3

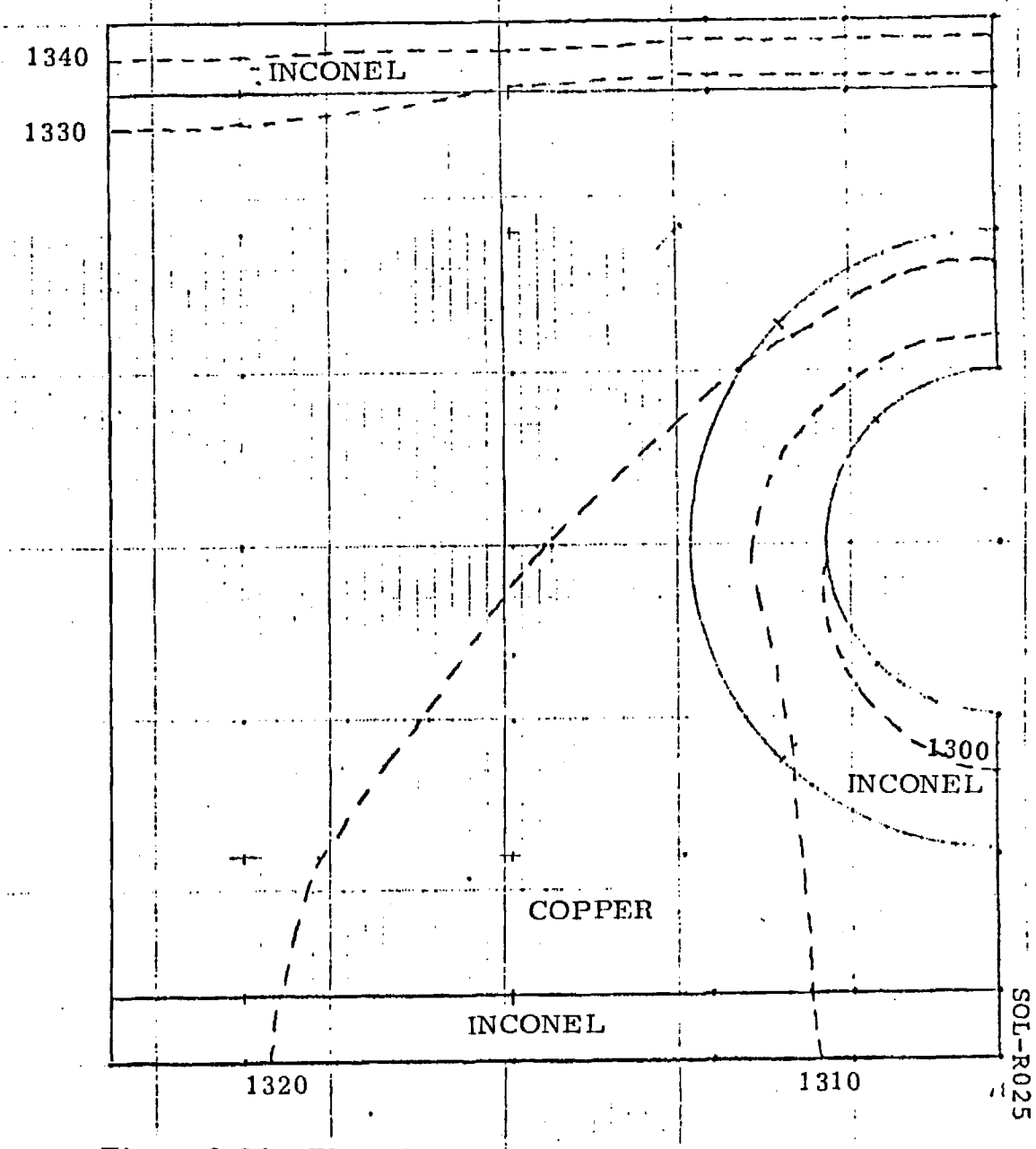

Cone Radius = 5.87"

Figure 2-2d. Plane 4

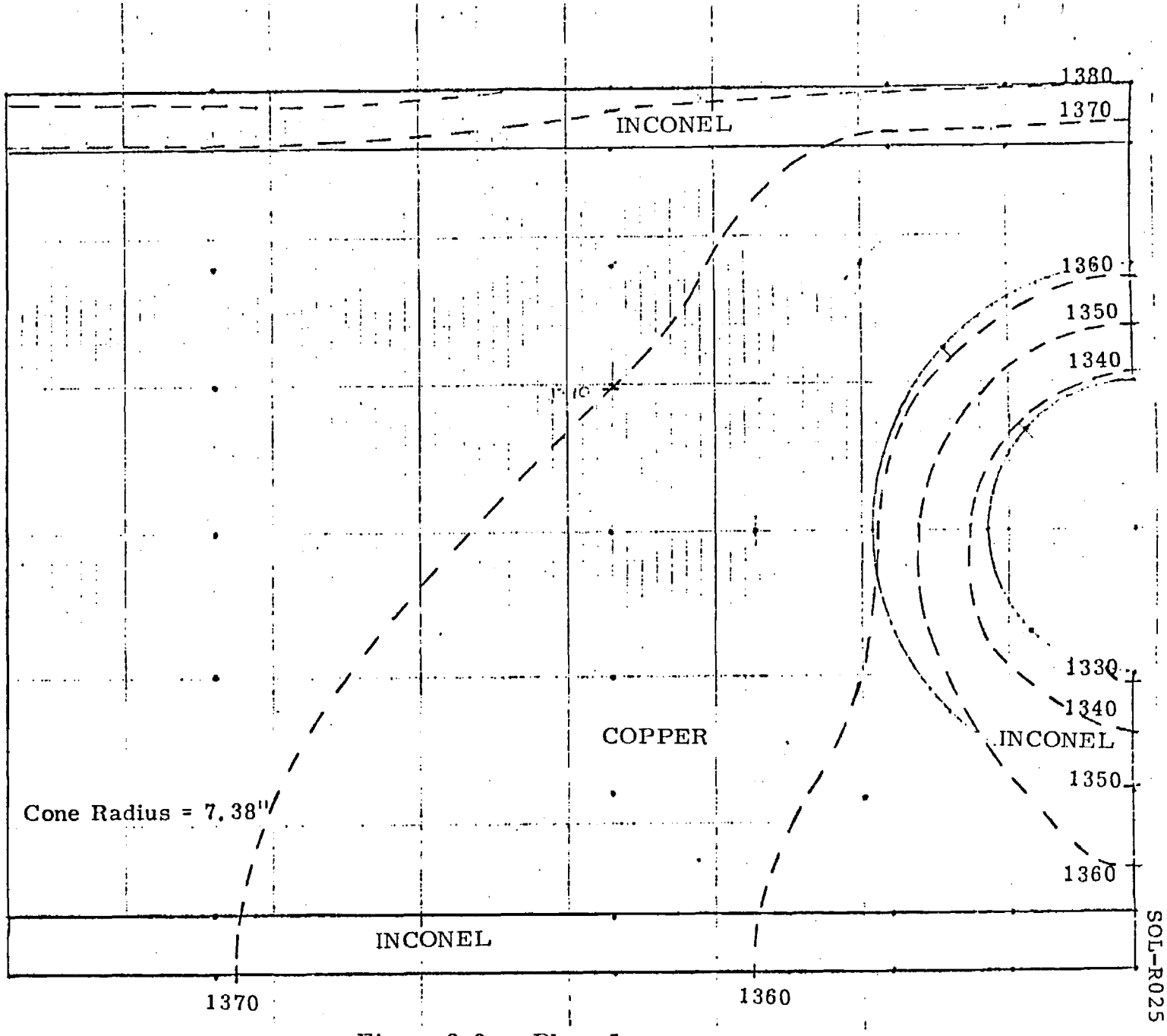

Figure 2-2e. Plane 5

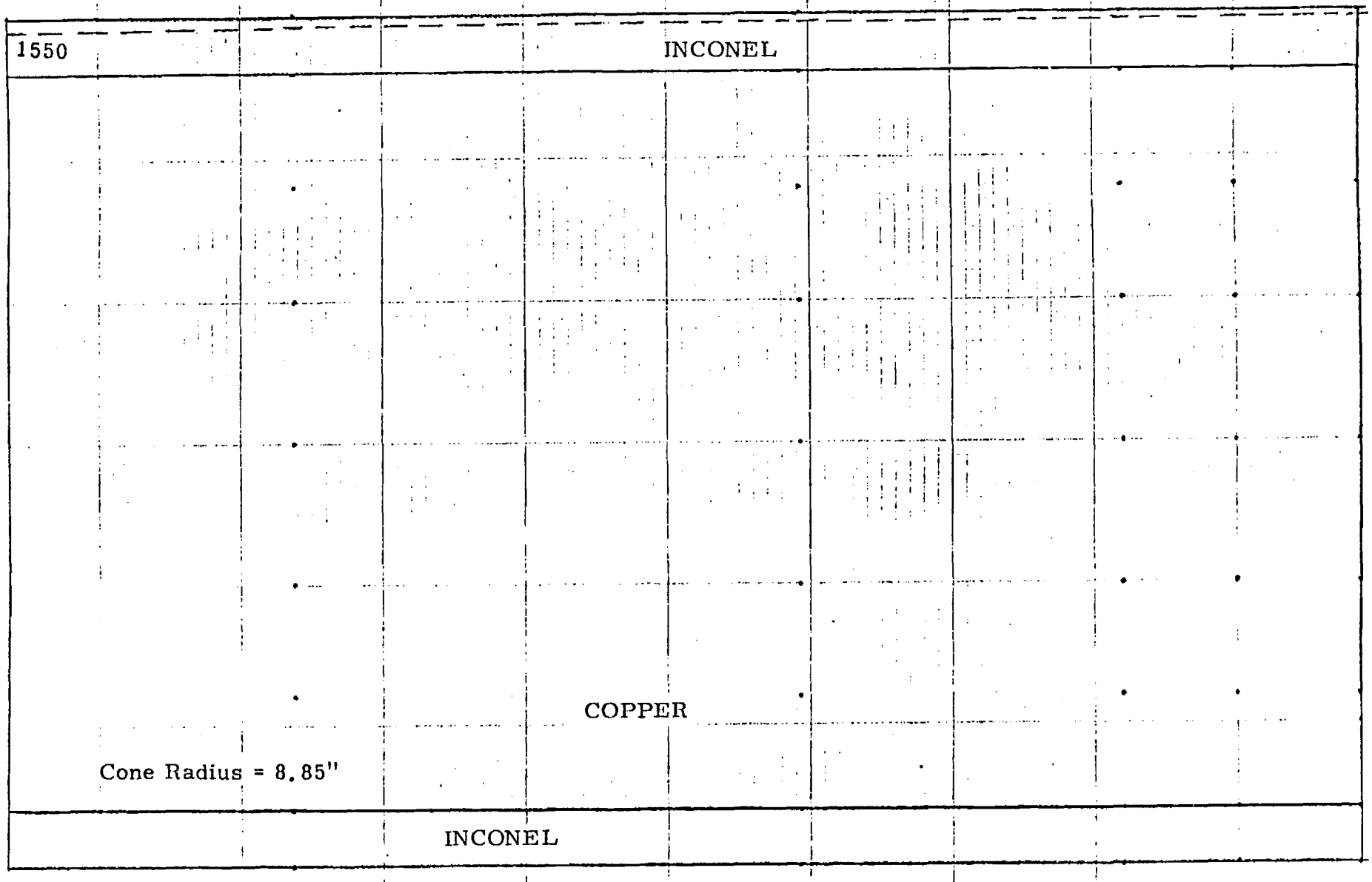

Figure 2-2f. Plane 6

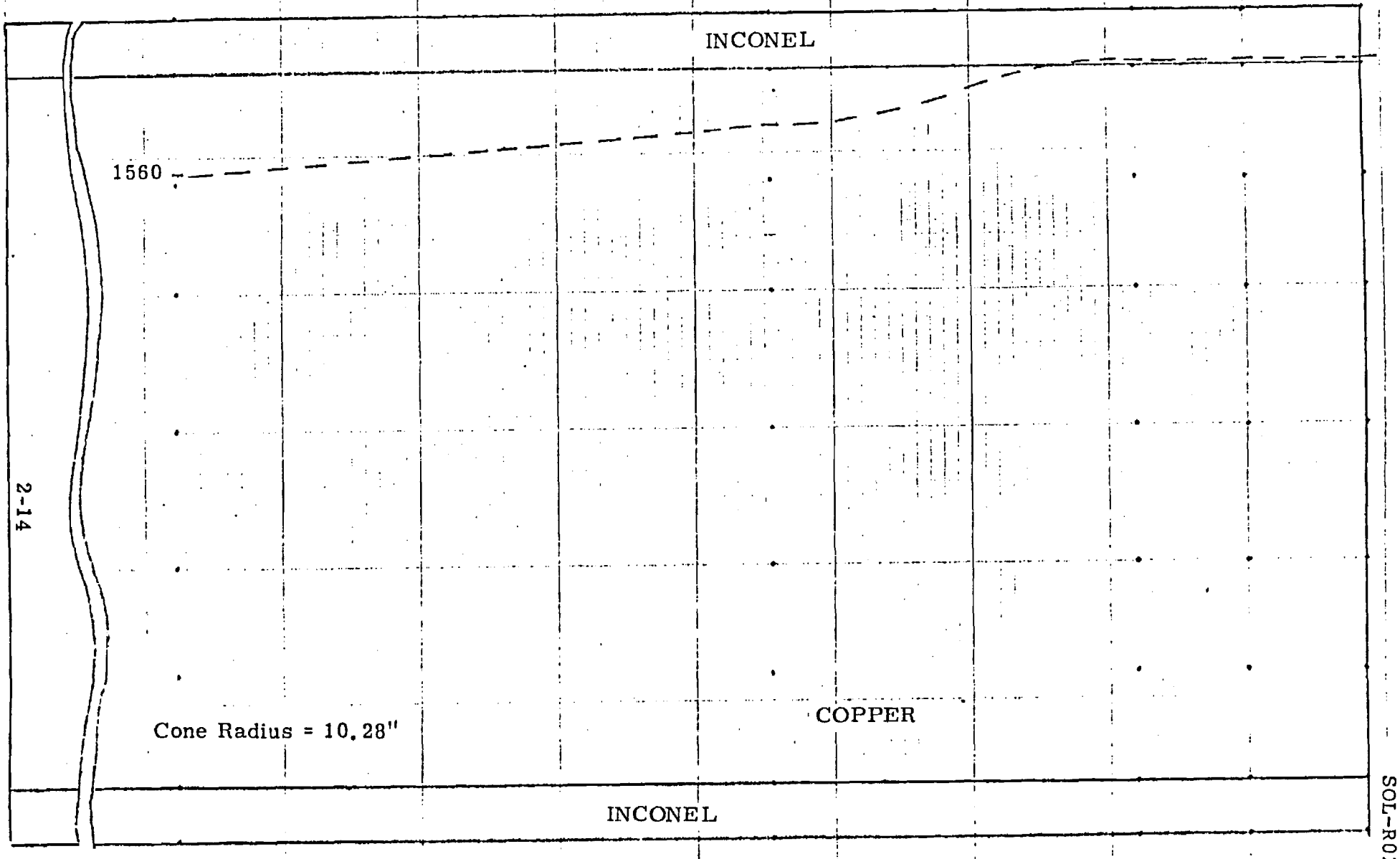

Figure 2-2g. Plane 7

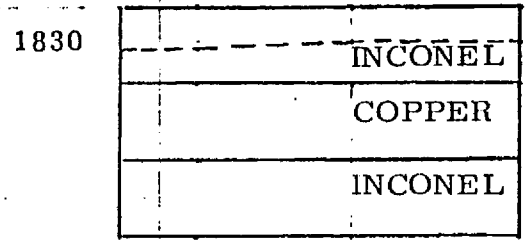

Cone Radius = 2.38"

Figure 2-3a. Plane 1

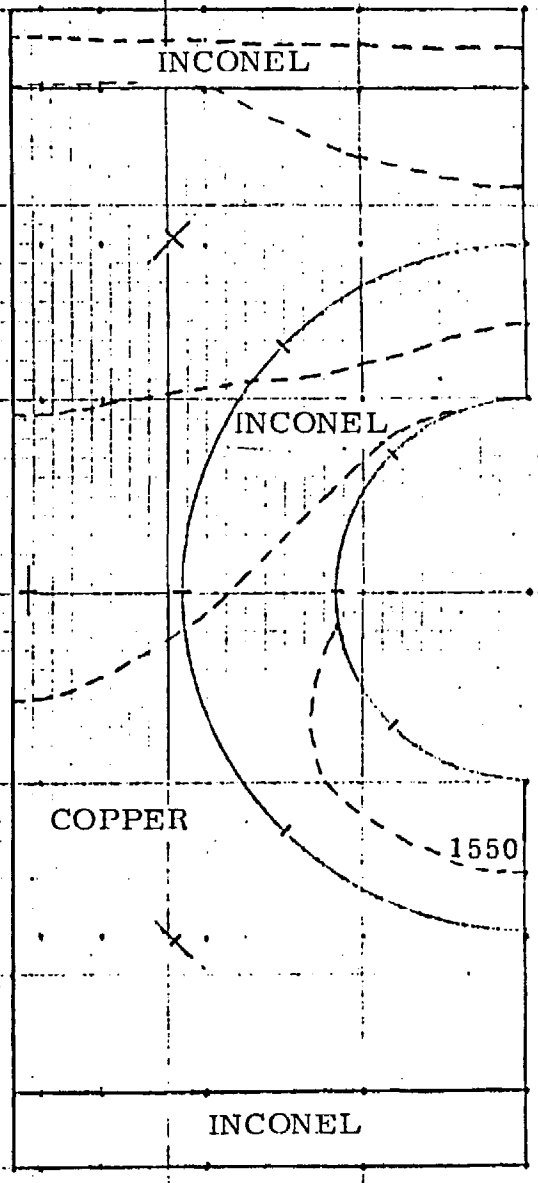

Cone Radius = 3.06"

Figure 2-3b. Plane 2

SOL-R025

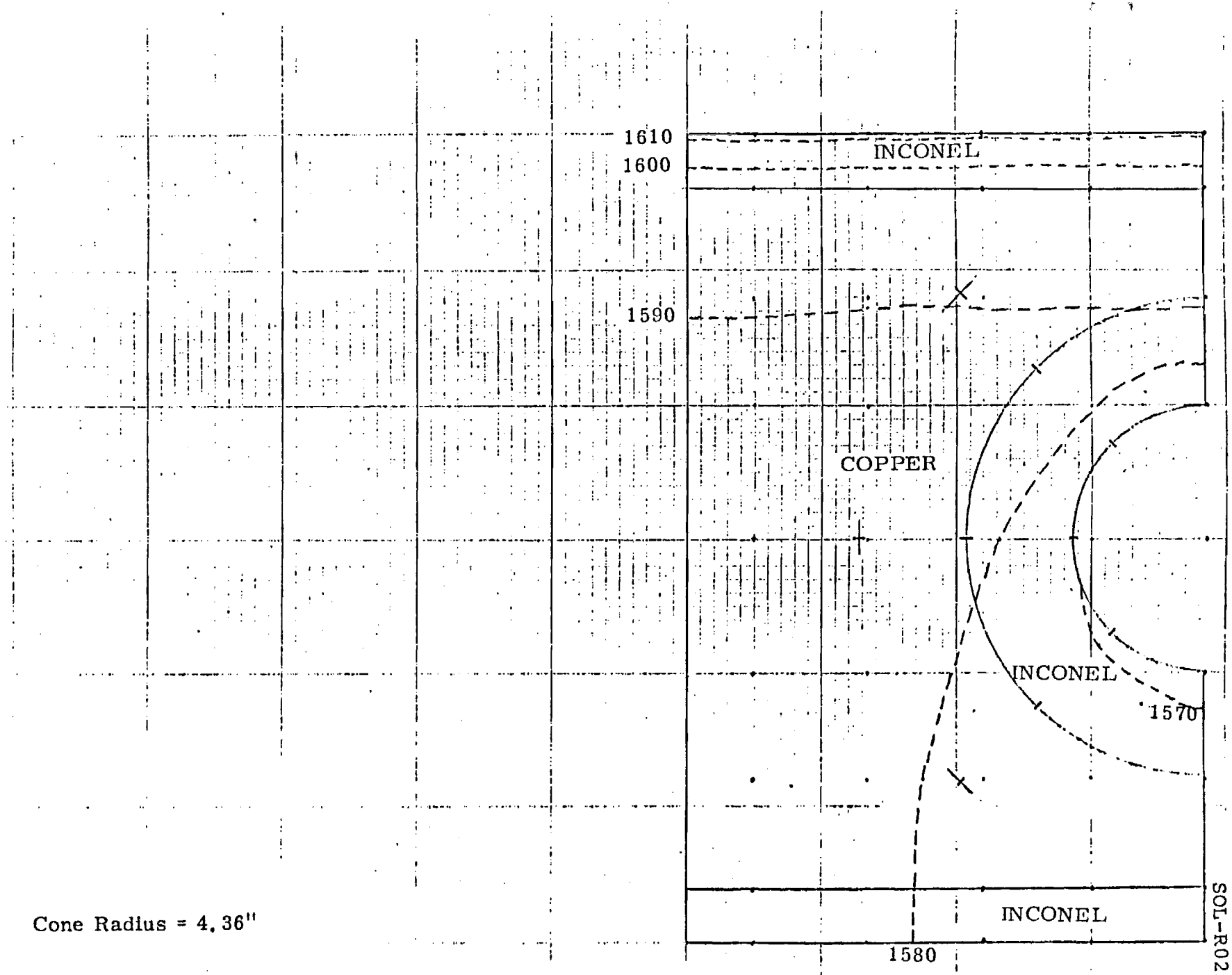

Cone Radius = 4.36"

Figure 2-3c. Plane 3

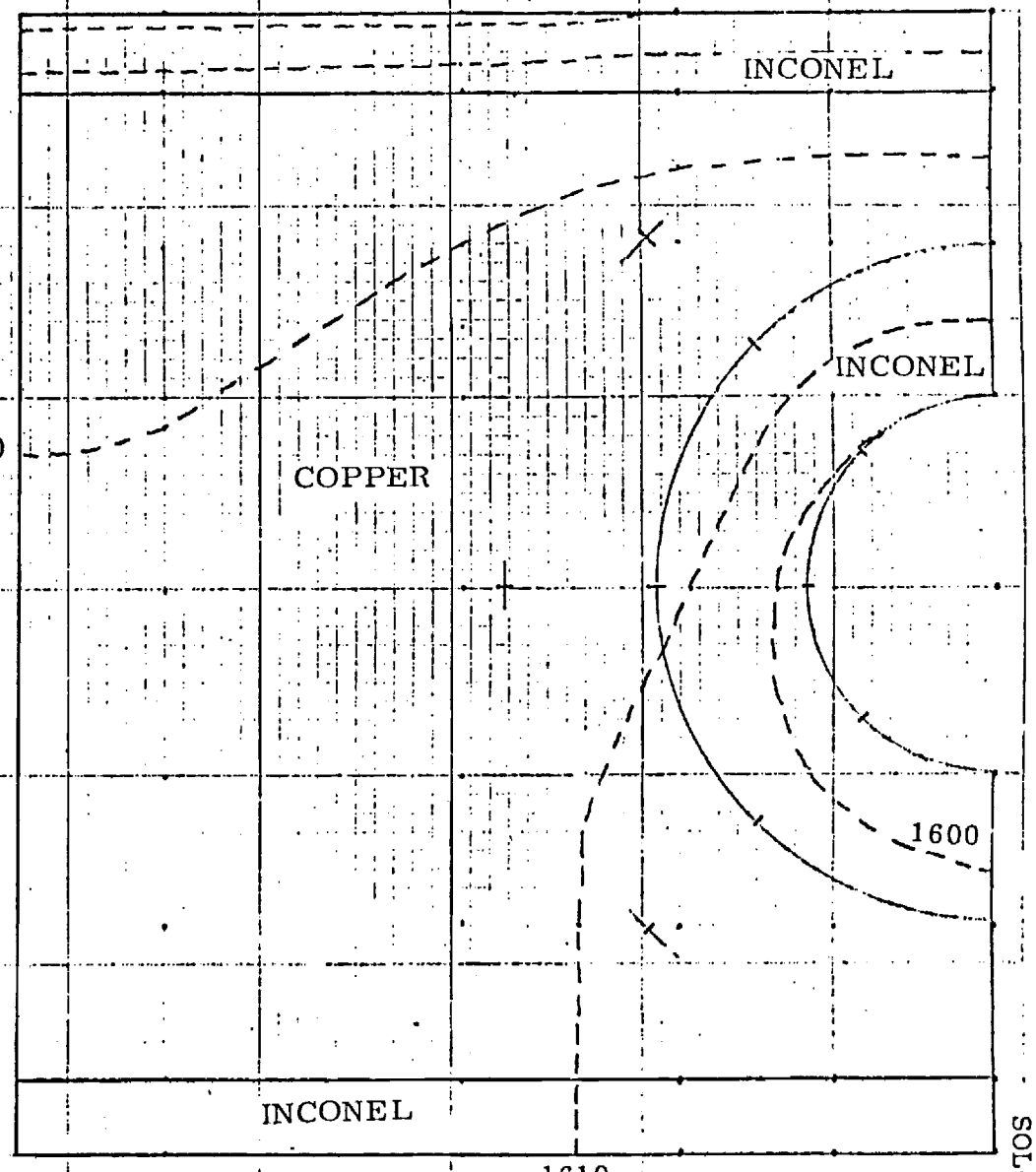

Cone Radius = 5.87"

Figure 2-3d. Plane 4

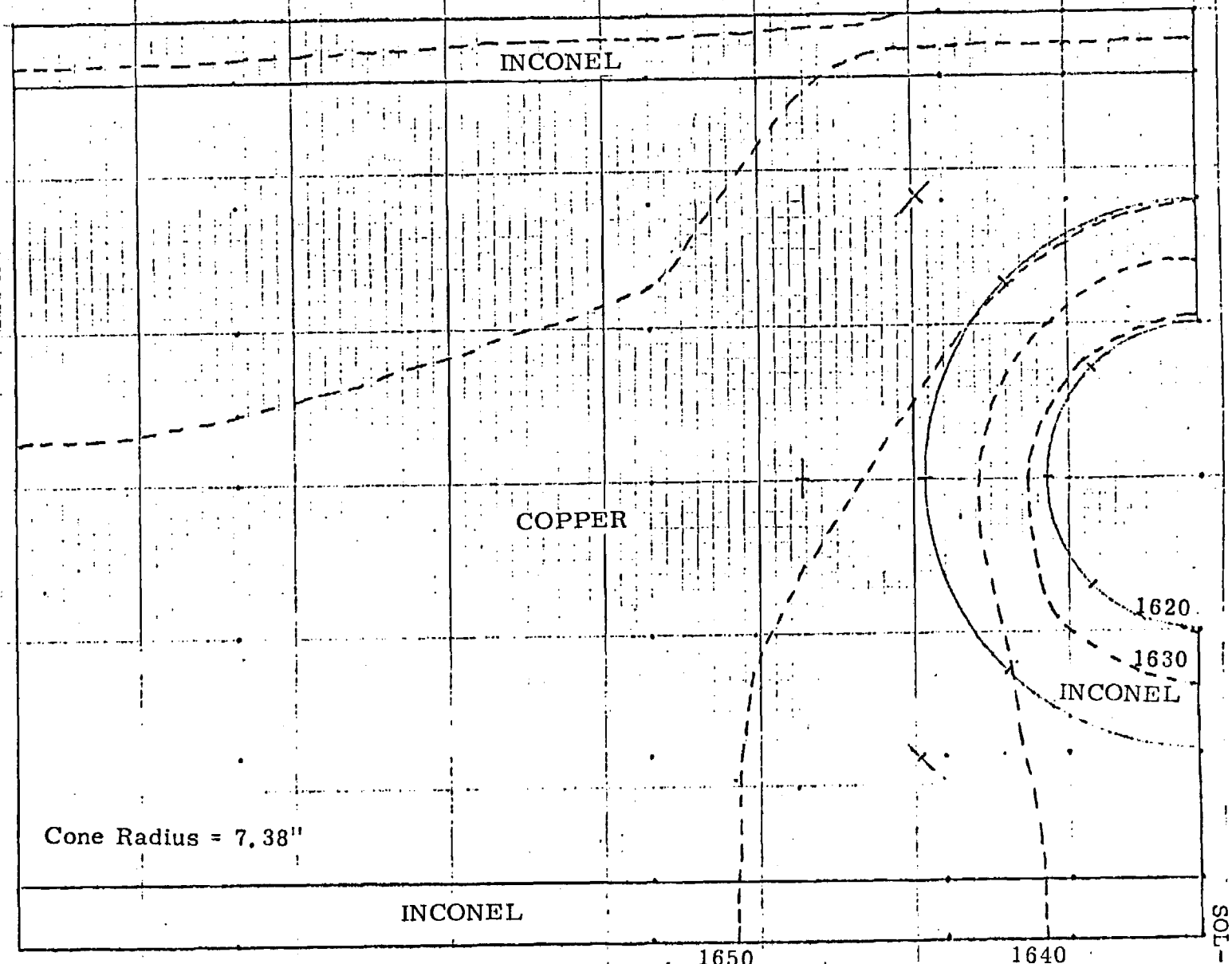

Figure 2-3e. Plane 5

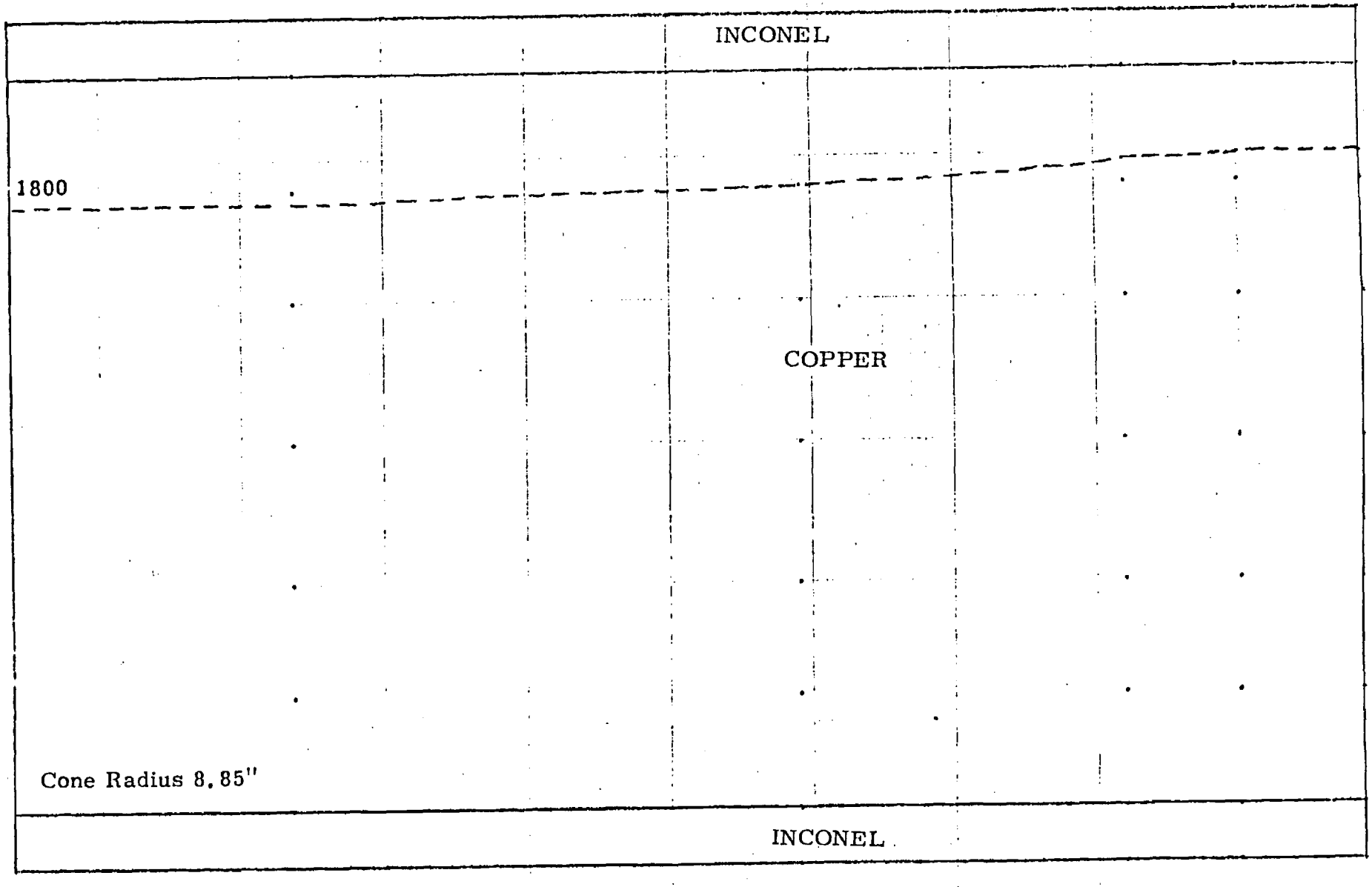

Figure 2-3f. Plane 6

SOL-R025

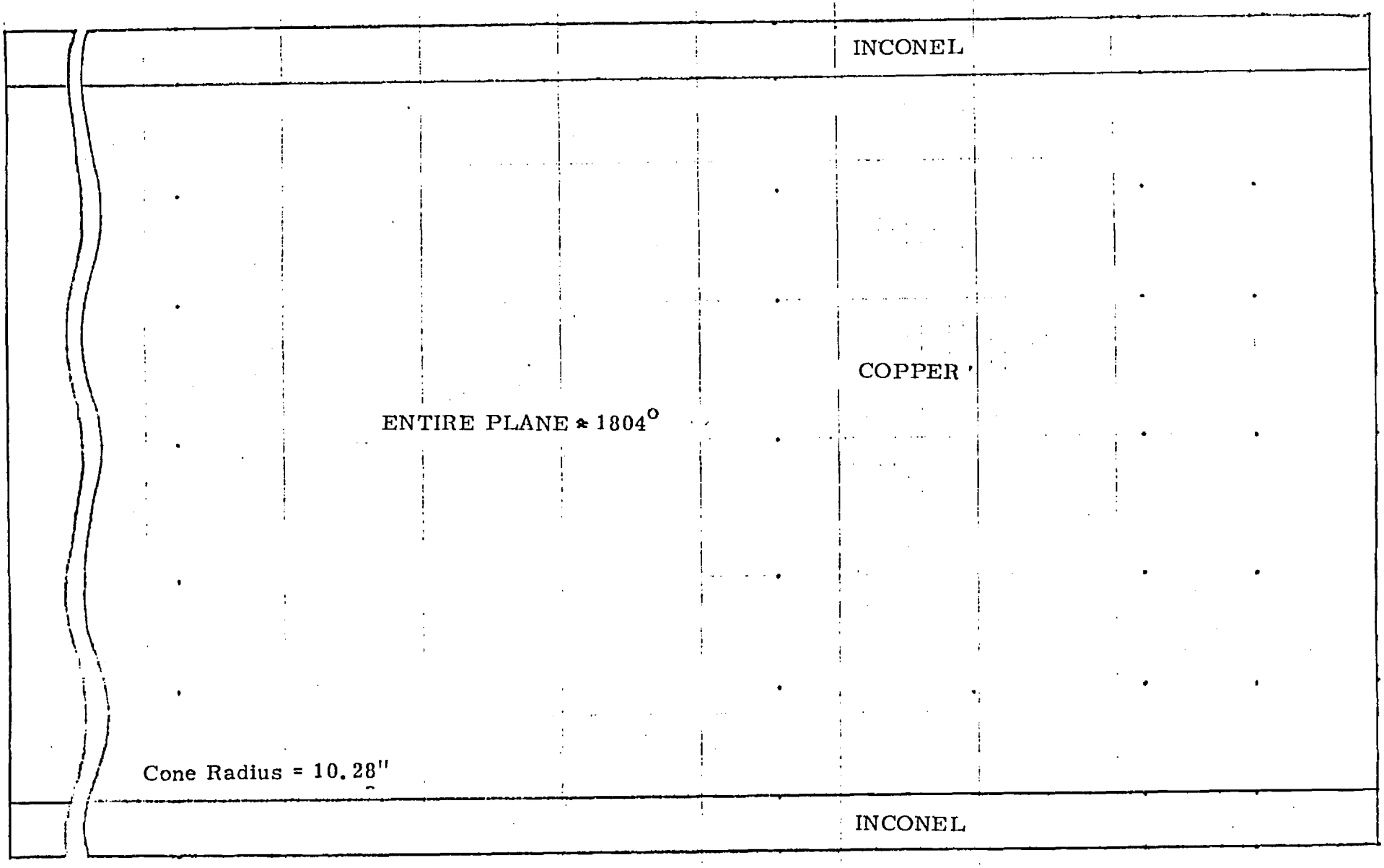

Figure 2-3g. Plane 7

Table 2-III Efficiency and Temperature Comparisons

The °F	Aperture Dia. (cm)	Aperture Plate Color	Plug Color	Cylinder Wall Color	T Cone Max (°F)	Aperture Plate Temp. (°F)	Plug Temp (°F)	Q_{He} (Kbtu/hr)
1328	28	White	White	Black	1693	1216	1985	190
1328	28	White	White	White	1721	1163	2003	195
1500	28	White	White	Black	1832	1321	2041	181
1328	28	White	Black	Black	1686	1248	3614	187
1328	28	Black	White	Black	1676	1657	1988	184
1200	21	White	White	Black	1577	1219	1963	191
1200	23	White	White	Black	1590	1195	1964	194
1200	24	White	White	Black	1592	1182	1970	195
1200	25	White	White	Black	1588	1170	1964	193
1200	27	White	White	Black	1587	1149	1949	193
1200	29	White	White	Black	1581	1129	1934	191
1200	31	White	White	Black	1572	1105	1916	190
1200	28	White	White	Black	1525	1160*	1838	195*

*Estimated values for masked TBC.

The receiver performance indicated in Table 2-III are somewhat lower than those presented at PDR for several reasons. First, the improvements to the model result in a lower efficiency prediction, primarily because of reflected solar flux and the correction to the aperture plate radiation conductance. Second, the helium passages do not extend quite as far out in the cone as the earlier design, and there is no longer double tubing beyond a 5.5. inches radius. This change in tubing configuration was clearly necessary, but it has resulted in a slightly lower efficiency. This may be less significant for the masked Test Bed Concentrator, which has a smaller flux pattern.

The other point of interest in Table 2-III is that the optimum aperture diameter is 24 cm instead of the 28-cm size indicated by the pre-PDR runs. This is true because the solar radiation reflected from the receiver depends upon aperture size.

2.3 DESIGN OF APERTURE PLATE AND CERAMIC PLUG

2.3.1 Aperture Plate

2.3.1.1 Materials

Slip-cast fused silica is the best material for the aperture plate. This material is relatively inexpensive and the plate will be easy to fabricate. Most importantly, it has been tested at very high solar flux levels in the focal plane of the French solar furnace, where it was undamaged in a 1-minute exposure.

The use of a clear fused silica plate as the inner portion of the aperture plate was considered. This would have the advantage of allowing more solar radiation to enter the receiver because of the high solar transmittance of clear fused silica. Synthetic clear fused silicas have better than 90-percent transmission from 0.23 μm to 2.7 μm. At 2.7 μm transmission goes to zero; it then rises from zero at 2.8 μm to 77 percent at 3.2 μm, then gradually tails off to zero between 4 and 5 μm. The synthetic vitreous silicas are produced by hydrolization of $SiCl_4$ in an oxygen-hydrogen flame or in a water-vapor-free plasma flame. Trade names for the materials produced in the O_2H_2 flame are: (1) Suprasil from the Amersil Division of Englehard Industries, (2) Spectrosil from the Thermal American Fused Quartz Company, and (3) Corning 7940 from the Corning Glass Company. Trade names for the water-vapor-free materials are Suprasil W, Spectrosil WF and Corning 7943. These fused silica glasses are extremely expensive and it is not likely to be feasible to purchase relatively large, thick sections of this material for use as an insert in a larger opaque fused silica aperture plate.

Normal fused quartz glass is prepared by electrical fusion under vacuum or an inert gas atmosphere of natural quartz. It may also be produced from quartz crystal powder in a flame fusion (Verneuille) process. Commercial names for the electrically fused products are: Infrasil (Amersil-Englehard), IR-Vitreosil (Thermal American) and General Electric's 105, 201 and 204. Commercial

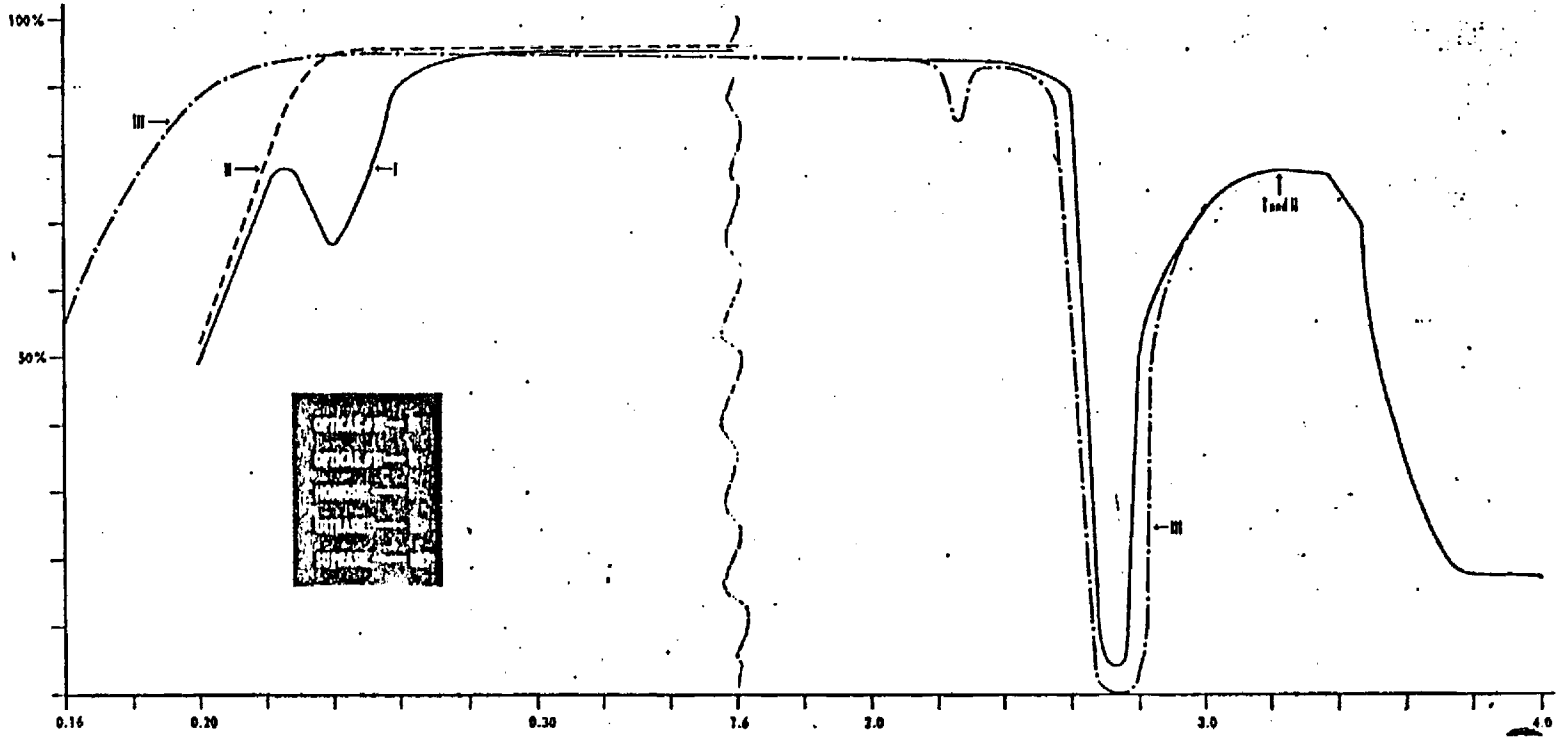

Figure 2-4. Percent Transmission of Entering Energy Excluding Surface Reflections (Measurements Made Through a 10-MM Thickness in Each Instance - Wavelength in Microns) Furnished by Englehard Industries, Inc.

flame-fused materials are: Herasil, Homosil, Optosil (Amersil-Englehard), O.G. Vitreosil (Thermal-American) and GE 104. The natural fused quartz materials have an absorption edge of 0.24 μm and reach 90 percent transmission at about 0.28 μm. There is a small absorption peak between 2.4 and 2.5 μm, but transmission drops only to 86 percent in this region, then returns to 92 percent. Figure 2-4 shows transmission for these different types of fused silica for ten mm thick specimens.

Beder, et al,[1] measured the transmissivity of fused quartz between 0.22 and 3.5 μm from room temperature to 1500°C. They found that the interval of virtual transparency (transmissivity $\gtrsim$ 85 percent) of each type of vitreous silica was reduced by heating caused by a shift in both the long and short wave length absorption edges. At 500° and 750°C transmissivity dropped below 85 percent at 2.4 μm. The 750°C heated material dropped to 0 transmissivity at 3.5 μm at a much more rapid rate than the 500°C heated material. Even with this drop in transmissivity, a cavity radiating at 1400°F would lose about 23 percent of the energy through the transparent fused silica. Some of the radiation loss could be reduced by metallizing the back face, as suggested in the JPL report[2]; however it is believed that the input energy gained by using a transparent center section is not worth the economic cost caused by complicating the design of the aperture plate. An aggregate cast fused silica plate 3/4-inch (1.9 cm) thick would be expected to transmit a very negligible

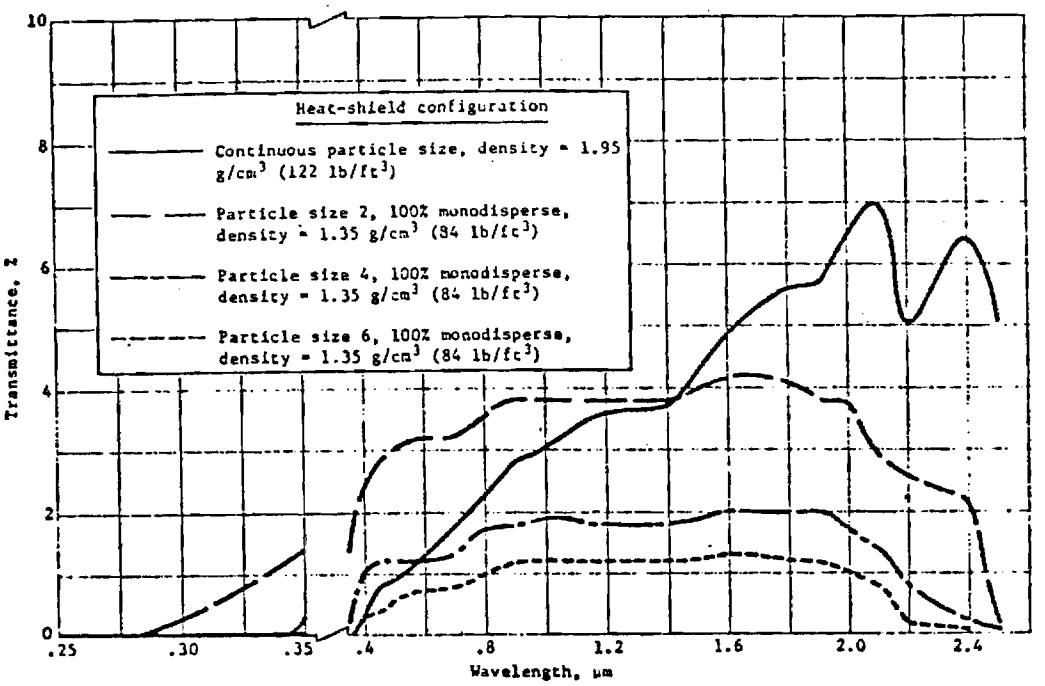

Figure 2-5. Spectral transmittance of 0.25-cm (0.10-in.) thick models of different slip-cast configurations made from GE 204 fused silica

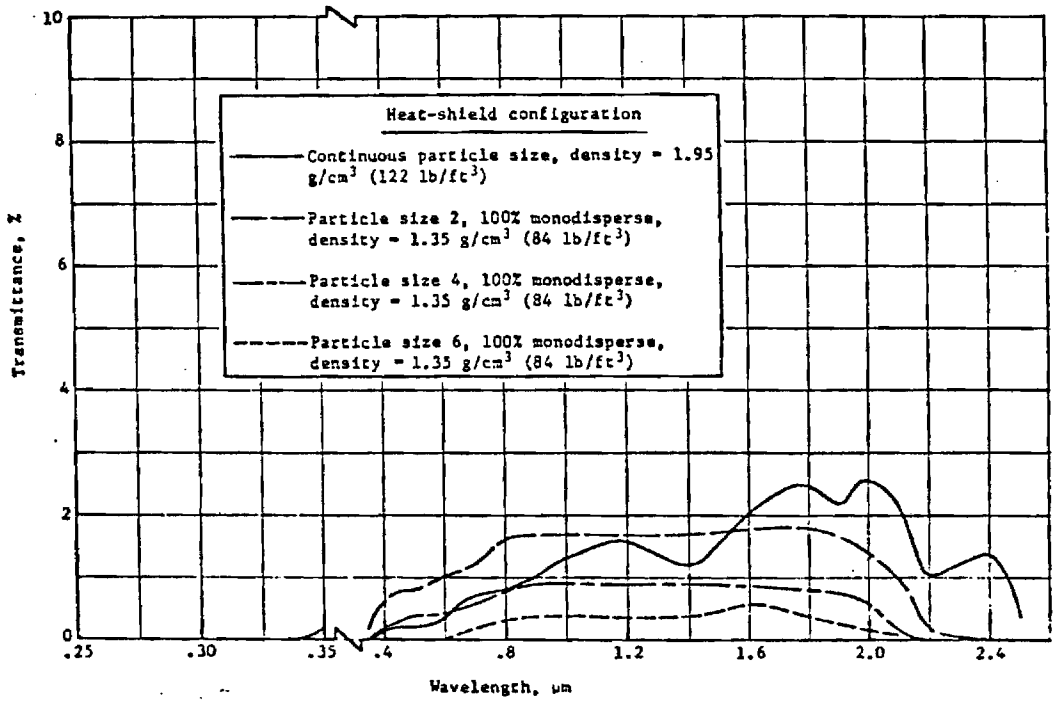

Figure 2-6 Spectral transmittance of 0.51-cm (0.20-in.) thick models of different slip-cast configurations made from GE 204 fused silica

amount of radiation, based on the Martin-Marietta measurements on high purity slip-cast fused silica specimens 0.1 and 0.2-inch thick[3]. These measurements are shown in Figures 2-5 and 2-6. It can be seen that the maximum spectral transmittance for the continuous distribution material for 0.10-inch material was 7 percent at 2.1 μm and was 2-1/2 percent for the 0.20-inch material at 2.0 μm. An extrapolation to 3/4-inch thick material would indicate almost no transmission. From the standpoint of economics, there is no questioning the fact that the aggregate cast plate would be much less costly than a clear fused silica plate. One unknown factor in the use of the aggregate cast plate is the effect of absorbed moisture, since the plate will have some porosity. With the plate facing downward, it should not get extremely wet from rain but, sufficient moisture could be absorbed to cause fracturing from steam pressure under very high heating rates. Since heating takes place on a diurnal cycle and temperature of the plate is expected to reach temperatures of the order of 1000°F, there is no economically effective way of sealing the plate against moisture penetration.

The Fairchild drawing indicates an approximate 1/2-inch-thick aperture plate. A 1/2-inch thick plate of aggregate cast fused silica, approximately 30-inches in diameter, would be very difficult to handle because of its low strength in the dry state. Even if it could be successfully transferred to the kiln, the chances are that it would severely warp during sintering.

The minimum thickness, by the fabrication constraints, will be between 3/4 and 1-inch. Every effort will be made to keep the thickness to 3/4-inch. To make the plate with rounded corners, as shown in the Fairchild drawing, would require an expensive machining operation. To keep the aperture thin, the plate can be cast with a tapered center plug to give the shape shown in Figure 2-7.

2.3.1.2 Attaching Aperture Plate to Remainder of Structure

The simplest method of holding the plate to the remainder of the structure is to provide a continuous metal rim around the periphery of the metal plate, overlapping the silica 1/2 inch. The metal "Z" section forming this lip must be detachable for insertion or removal of the silica aperture plate. A detail of this rim formed from 1/8-inch steel is shown in Figure 2-8.

Thermal expansion differences between the silica and the metal require that some method must be provided to keep the silica plate properly located and tightly held in position at ambient and operating temperatures. A 1/2-inch-thick, 3-lb/ft^3 (pcf) alumino-silicate fiber blanket, such as Kaowool or Fibrefax, should be wrapped around the edge of the plate. A gasket of the same material, 3/4-inch-thick, should be placed on top of the plate in the area to be covered by the metal rim. Bolting the metal "Z" section in place will require a total force of about 150 to 220

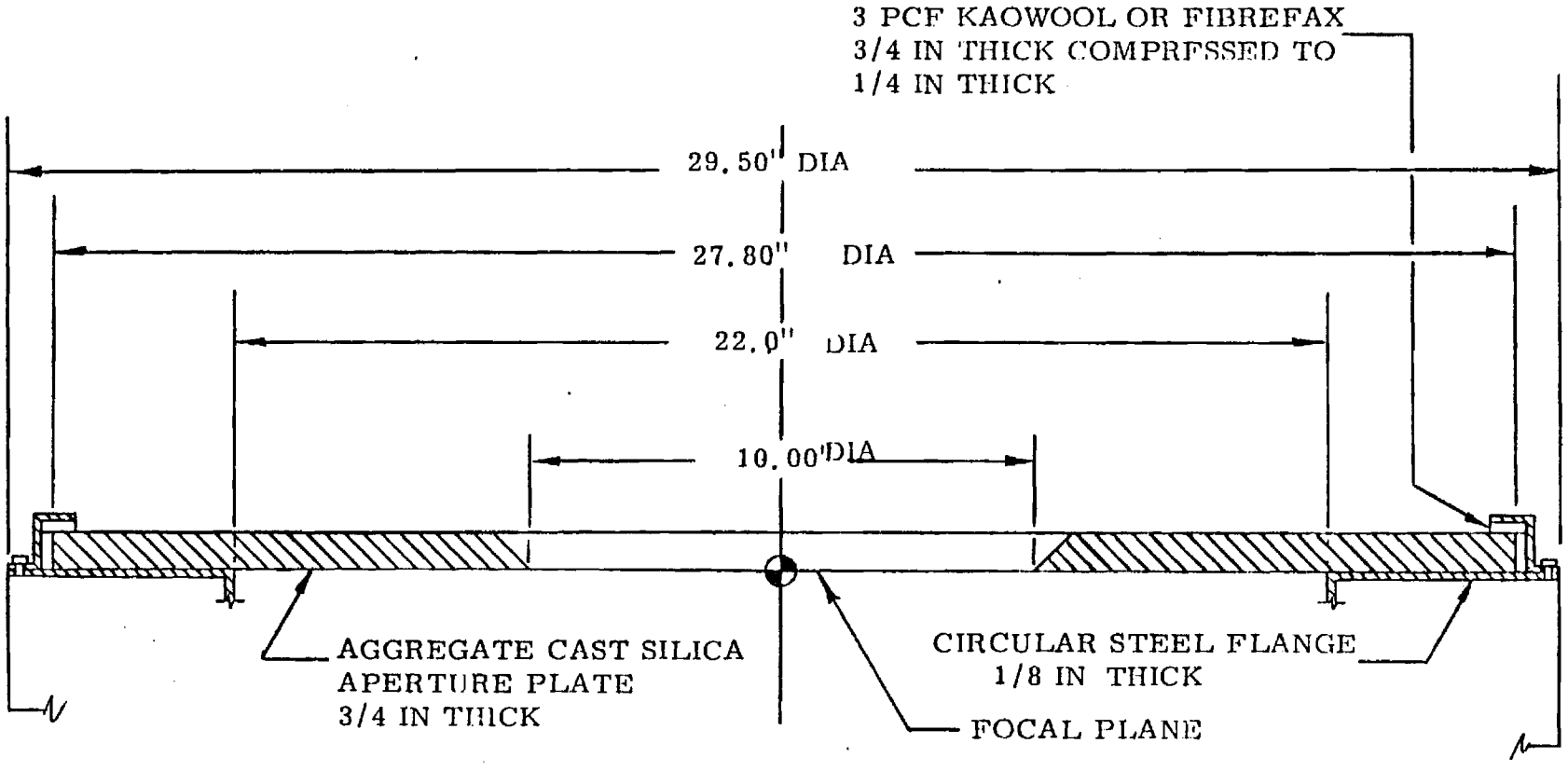

Figure 2-7. Aperture Plate (Advanced Concentrator)

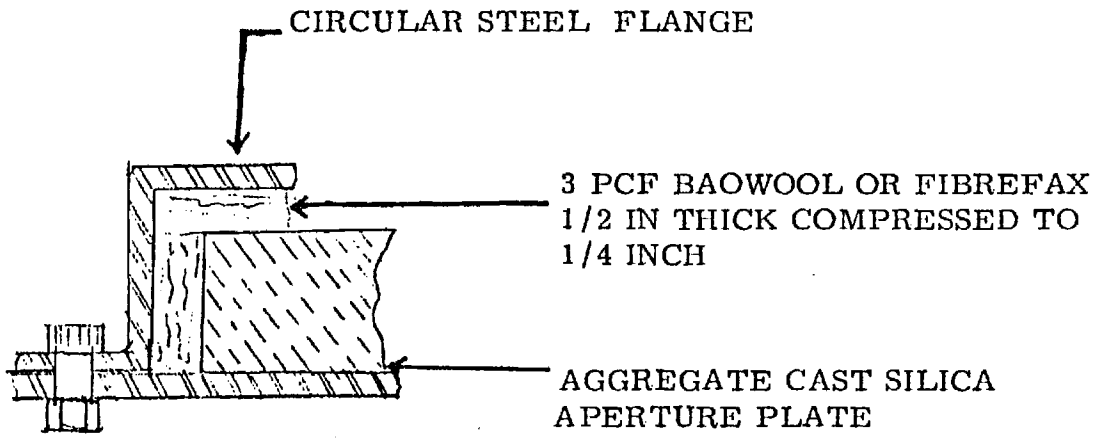

FULL SCALE

Figure 2-8. Aperture Mounting Arrangement

pounds to compress the ceramic fiber blanket to 1/4-inch thickness. This will firmly hold the aggregate cast fused silica aperture plate in position.

An estimate of the diametral expansion difference between the metal rim and the silica plate for a 200°F temperature rise is:

$$(\alpha_{steel} \times \Delta T \times D_{steel\ rim}) - (\alpha_{SiO_2} \times \Delta T \times D_{aperture\ plate})$$

$$\left(\frac{8 \times 10^{-6}}{°F} \times 200°F \times 30.2 \text{ in.}\right) - \left(\frac{3 \times 10^{-7}}{°F} \times 200°F \times 29.5 \text{ in.}\right)$$

$$= 0.045 \text{ in.}$$

The compressed fiber blanket on the edge of the plate should have sufficient resilience to handle this small expansion and keep the aperture plate centered.

Expansion in the vertical direction should be neglibible:

$$(8 \times 10^{-6} \times 200 \times 1) - (3 \times 10^{-7} \times 200 \times 0.75)$$

$$= 0.0016 \text{ inch.}$$

2.3.2 Ceramic Plug

The design shown in the Fairchild drawing needs minor modification. This area will receive a lot of heat and the bolt head will need protection. The major problem with the design is a method to keep the plug from becoming loose from the thermal expansion of the bolt. Because of space limitations on the underside, the only method of maintaining tension on the bolt is to

place a waved washer under the bolt head. This must be of a material which will retain "springiness" at the operating temperature of the ceramic plug.

It is recommended that the slot in the ceramic plug be cut slightly to accommodate the waved washer(s). It might be advisable to fabricate a ceramic part to fit in the slot above the bolt head. This part should be of the same material as the ceramic plug so that thermal expansions match. The plug must fit snugly to prevent radiation from reaching the bolt head, but must be relatively easy to remove to allow tightening or removal of the bolt. The bolt and waved washers must be fabricated from refractory metals such as stainless steel and Tantalloy to withstand the potential 1800° to 1900°F temperature that may be reached within the plug during operation. If Tantalloy is used for the waved washers, they will have to be plated. FSD Report No. SOL-R017, page 2-82, suggests that the center plug be of fused silica with Sialon as a back-up. The report does not specify the type of fused silica, but clear fused silica would be unacceptable for the same reasons as delineated for the aperture plate. Slipcaste or aggregate cast fused silica should be satisfactory for this plug, provided there are no large physical stresses unknown at this time. Sialon is unacceptable because of its dark color, hence high absorptivity. It would operate at a much higher temperature than the slip-cast fused silica (SCFS). Also Sialon is reported to have a thermal conductivity of 12 Btu/ft-hr-°F[5], which is about 24 times that of SCFS

(0.5 Btu/ft-hr-°F)[6]. This would result in excessive heating of the mounting bolt and washers.

Experience at the French solar furnace in April showed that a 1-inch-diameter x 1/2-inch-thick GE Sialon material failed rapidly in thermal shock. Under a solar incident flux of 226 cal/cm^2-s, the Sialon surface "exploded" in 0.7 seconds with complete failure in 1.6 seconds. Based on previous experience with other solar applications, Cordierite is recommended as the back-up material for the ceramic plug. Cordierite ($2MgO \cdot 2Al_2O_3 \cdot 5SiO_2$) has a light cream to white color, has a flexural strength of 125 MN/m^2, a tensile strength of 32MN/m^2, a thermal conductivity of 0.006 cal/cm·s·°C and a thermal expansion of 1.5 x 10^{-6}/°C at 100°C, 2.5 x 10^{-6}/°C at 500°C. The combination of strength and low thermal expansion and conductivity make this material resistant to thermal shock. No emissivity data are available but the material is not expected to absorb much solar radiation. Cordierite is a relatively low-priced ceramic and is relatively easy to machine. It can also be slip-cast to rough shape and finished by grinding by Coors Porcelain Company, Golden, Colorado.

The insulation scheme around the ceramic plug shown in the Fairchild PDR drawing appears satisfactory.

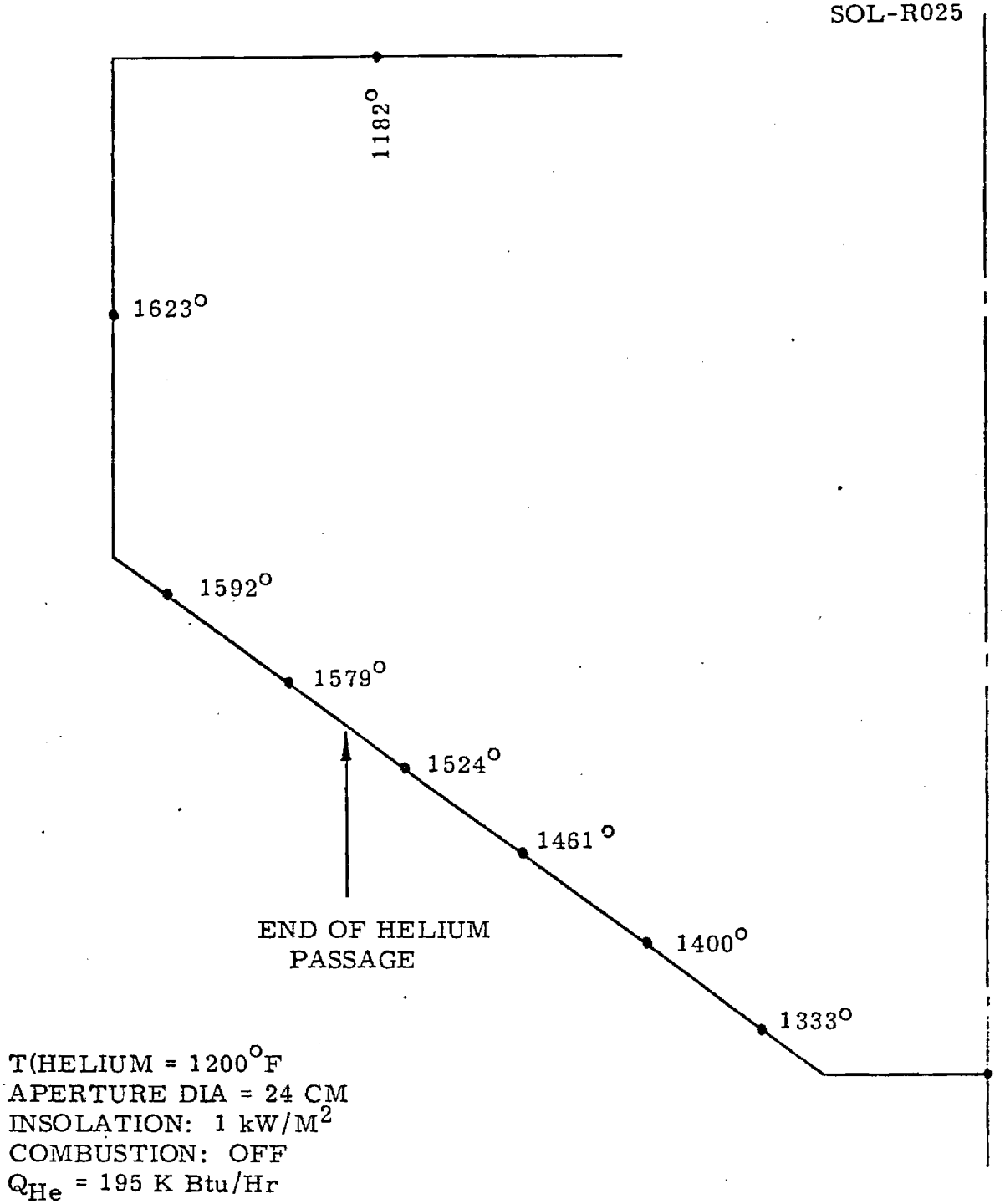

Figure 2-9. Cavity Surface Temperatures in 17 Node Model

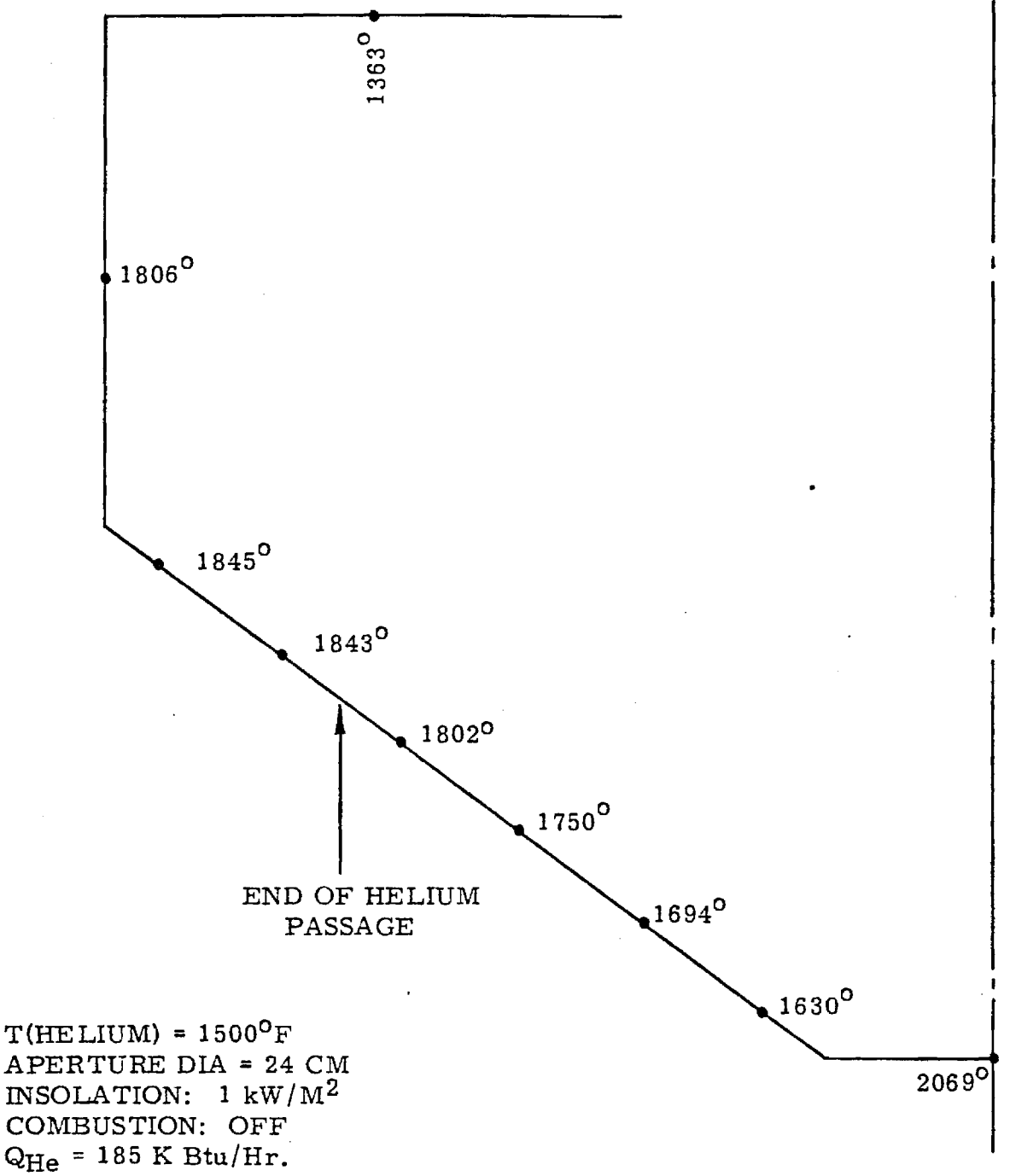

Figure 2-10. Cavity Surface Temperatures in 17 Node Model

2.4 MITAS MODELS

2.4.1 Comparison of 1200° and 1500°F Helium Temperature Models

Table 2-III does not show a direct comparison of 1200° and 1500°F helium models with a 24-cm diameter, which now appears to be the optimum size. The following Figures 2-9 and 2-10 provide this comparison.

2.4.2 Additional Data from 323 Node Models

The 323-node models predict slightly higher efficiencies than do the 17-node models and, in general, also predict lower temperatures. Confidence in the 323-node model is much higher. Figures 2-11 and 2-12 show temperatures and heat delivered to helium for 1200° and 1500°F helium temperatures.

Unfortunately, these models had 28-cm apertures, so comparison with Figures 2-9 and 2-10 is not quite a direct one. From Table 2-III, the Q_{He} shown on Figures 2-11 and 2-12 would be expected to increase about 2 percent if the aperture size were reduced.

The 323-node models also do a much better job of modeling the area where the helium passage leaves the cone and goes to the cylinder manifold. The portion of the cone inside this point becomes the hottest part in the 1500°F model.

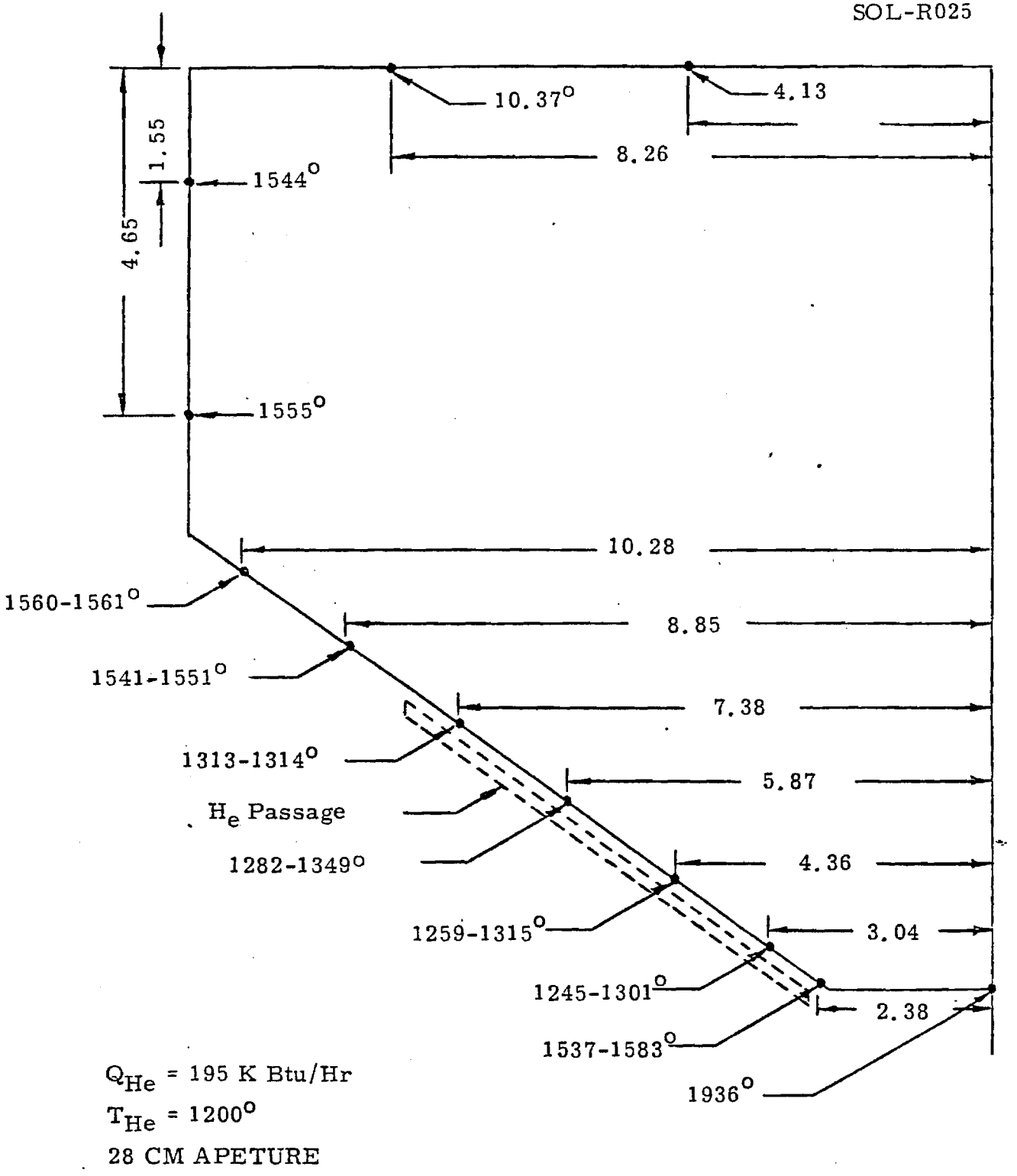

Figure 2-11. Temperatures in 323 Node Model

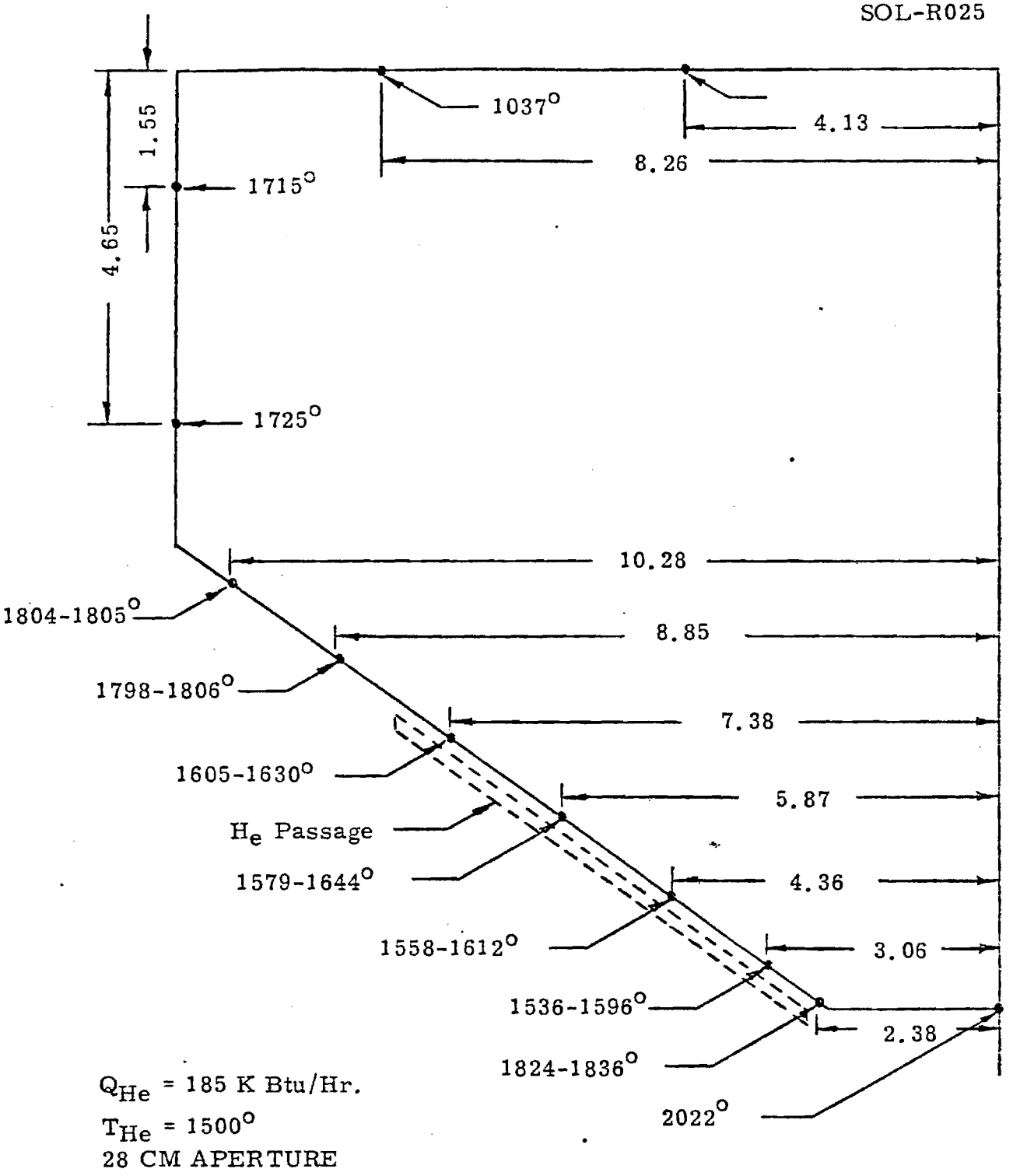

Figure 2-12. Advanced Concentrator Temperatures in 323 Node Model

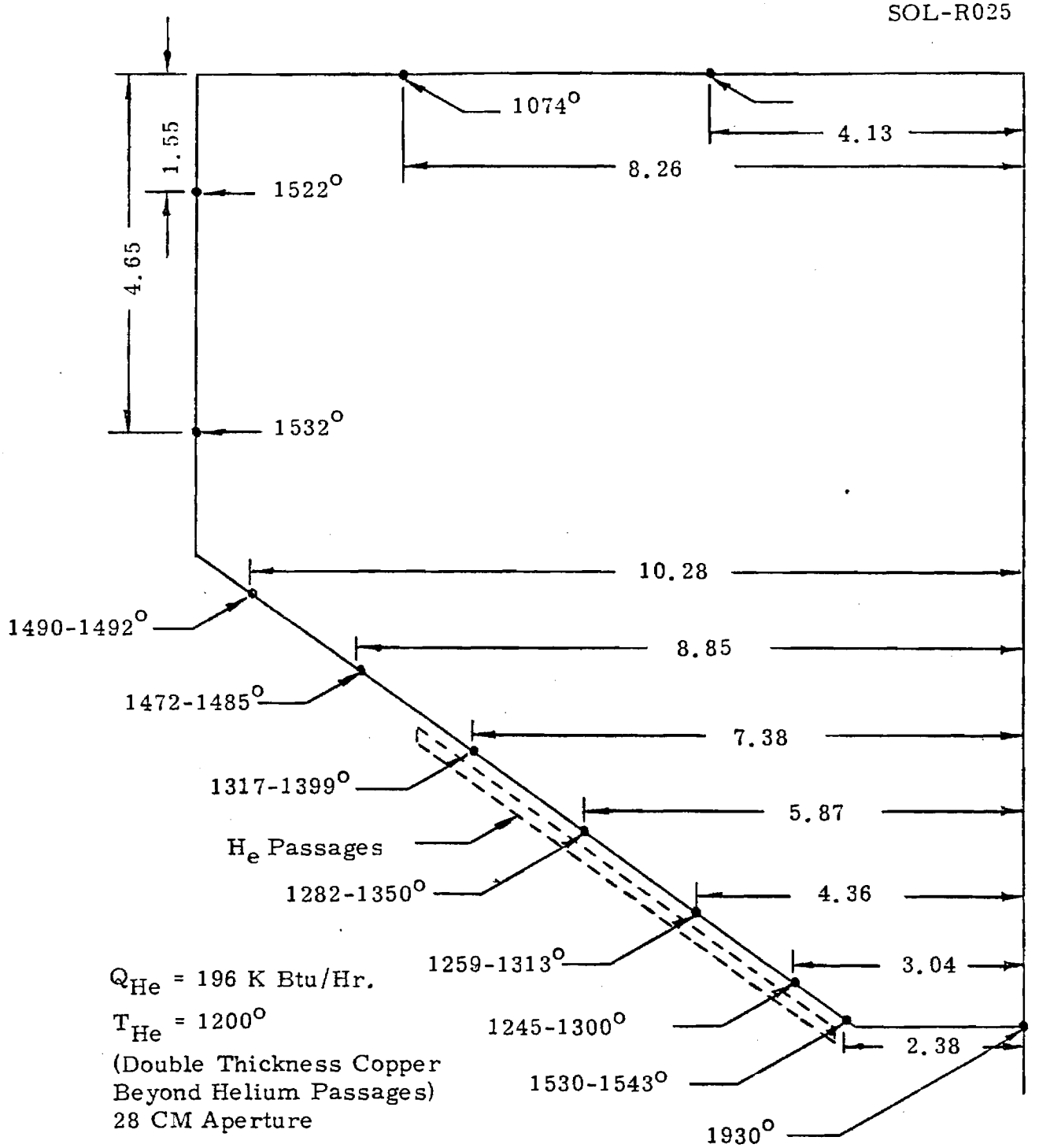

Figure 2-13. Advanced Concentrator Temperatures in 323 Node Model

An additional run was made to see if the addition of more copper beyond the radius at which the regenerator tube leaves the cone would be effective. For this model, the copper thickness was doubled beyond the regenerator tubes. The results are shown in Figure 2-13. A comparison of Figures 2-11 and 2-13 indicates that thicker copper will substantially lower the temperatures in the uncooled part of the cone. A slight improvement in efficiency will also be realized.

2.4.3 Critical Bend Area Model

A model was devised to analyze the area where the regenerator tube leaves the cone, primarily to determine the temperature gradients in the high stress areas. This was an extremely difficult model to prepare, even by making the simplification that the tubing bends abruptly and at a 90-degree angle. The tubing bend is actually more than 90 degrees and is not abrupt, so possibly the inaccuracies in the model will have some tendency to cancel. Results are shown in Figure 2-14.

2.4.4 Receiver Performance Specification

On the basis of the optical and thermal analyses, a Receiver Performance Specification was prepared. The numbers in the Table 2-IV were derived from the unthickened 323-node models, with corrections made for aperture size. The following cautions should be applied in using the results of this table:

1. The aperture size should be further reduced if the receiver is to be operated with the masked Test Bed

Table 2-IV. Expected Receiver Performance

(24-cm Aperture Diameter-Conduction Losses Not Included)

Advanced Concentrator

Parameter	1200°F He	1500°F He
Incident Flux (kW)	67	67
Aperture Interception	1.4	I.4
Energy into Helium (kW)	58.6	55.4
Energy into Helium (million Btu/hr)	0.2	0.189
Maximum Temperatures (°F)		
Center Plug	1966	2053
Cone	1561	1836
Outer Wall	1555	1725
Aperture Plate	1138	1234
Losses (kW)/(M-Btu/hr)		
Radiation	2.8/0.0096	5.2/0.018
Reflectance	0.9/0.003	0.7/0.002
Convection	3.6/0.0122	4.4/0.0151
Efficiency	0.875	0.827

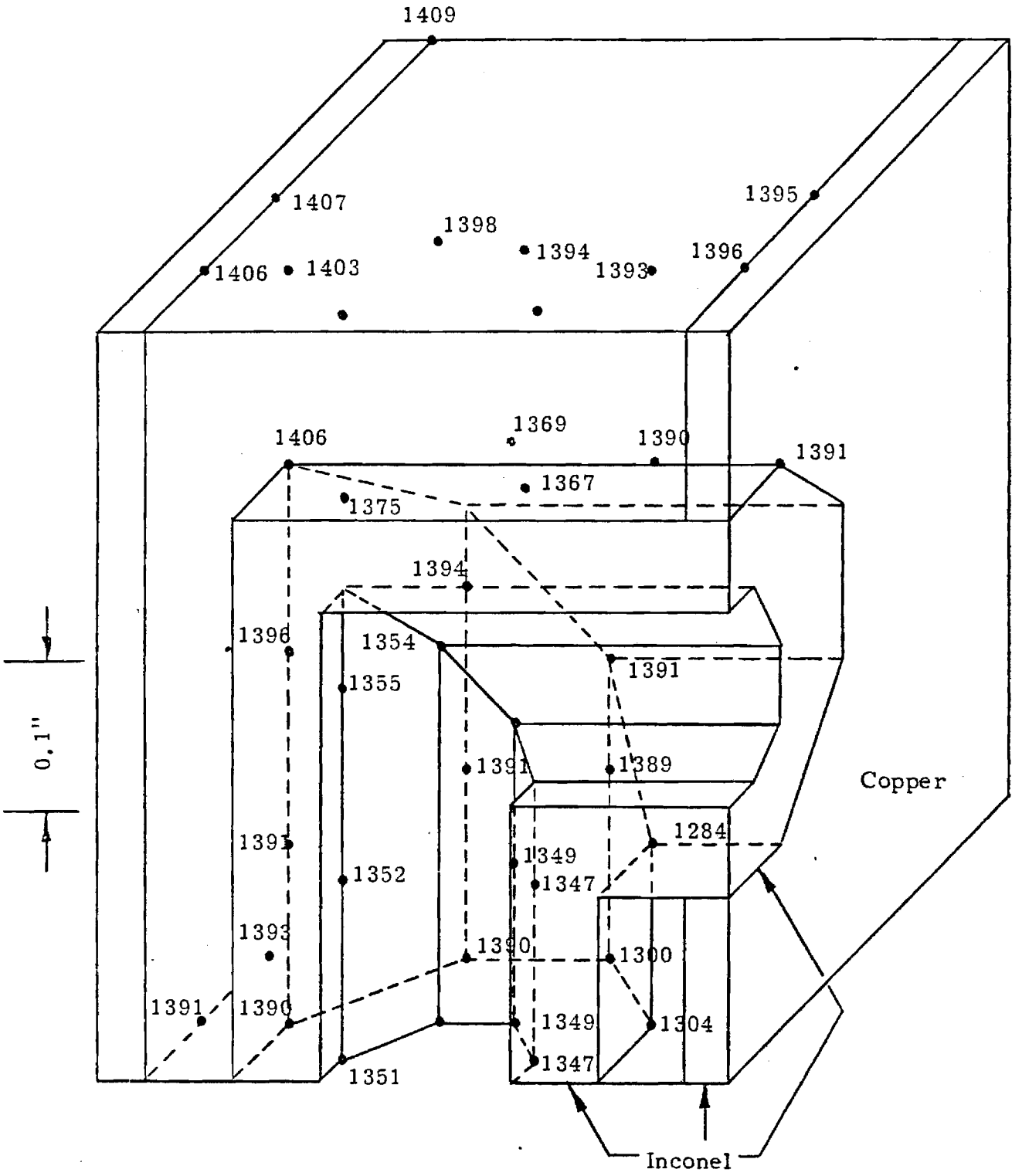

Figure 2-14. Temperatures in Bend Area (°F)

Concentrator. This has not been studied in detail, but it is expected that a 16-cm aperture size would be more nearly optimum for that concentrator.

2. Because of different flux pattern from the TBC, temperatures and efficiencies will differ from the values presented. From the one 17-node model of this configuration, it appears that the outer part of the cone will be cooler and that the efficiency will be higher.

SECTION 4.0

AIR PREHEATER DESIGN

The air preheater will utilize the hot exhaust gases from the combustor to preheat the incoming combustion air. The preheater concept, shown in Figure 4-1, consists of radial partitions located in the annulus between the inner cavity surface and concentric outer surface. These partitions form a series of alternate passages through which the incoming combustion air and combustion exhaust gases flow. Thus the preheater is a counterflow heat exchanger in which heat is transferred from the combustion exhaust gases to the incoming air through the partition walls. A design analysis was performed in order to determine the required number and size of partitions.

The geometry and nomenclature used for the preheater are shown in Figure 4-1. Details of manifolds which would distribute the exhaust gases and incoming air around the circumference are now shown, but it is assumed that both the incoming air and exit gases are evenly distributed over the series of passages.

The number and size of required partitions is determined from heat transfer consideration. The rate of heat transfer from

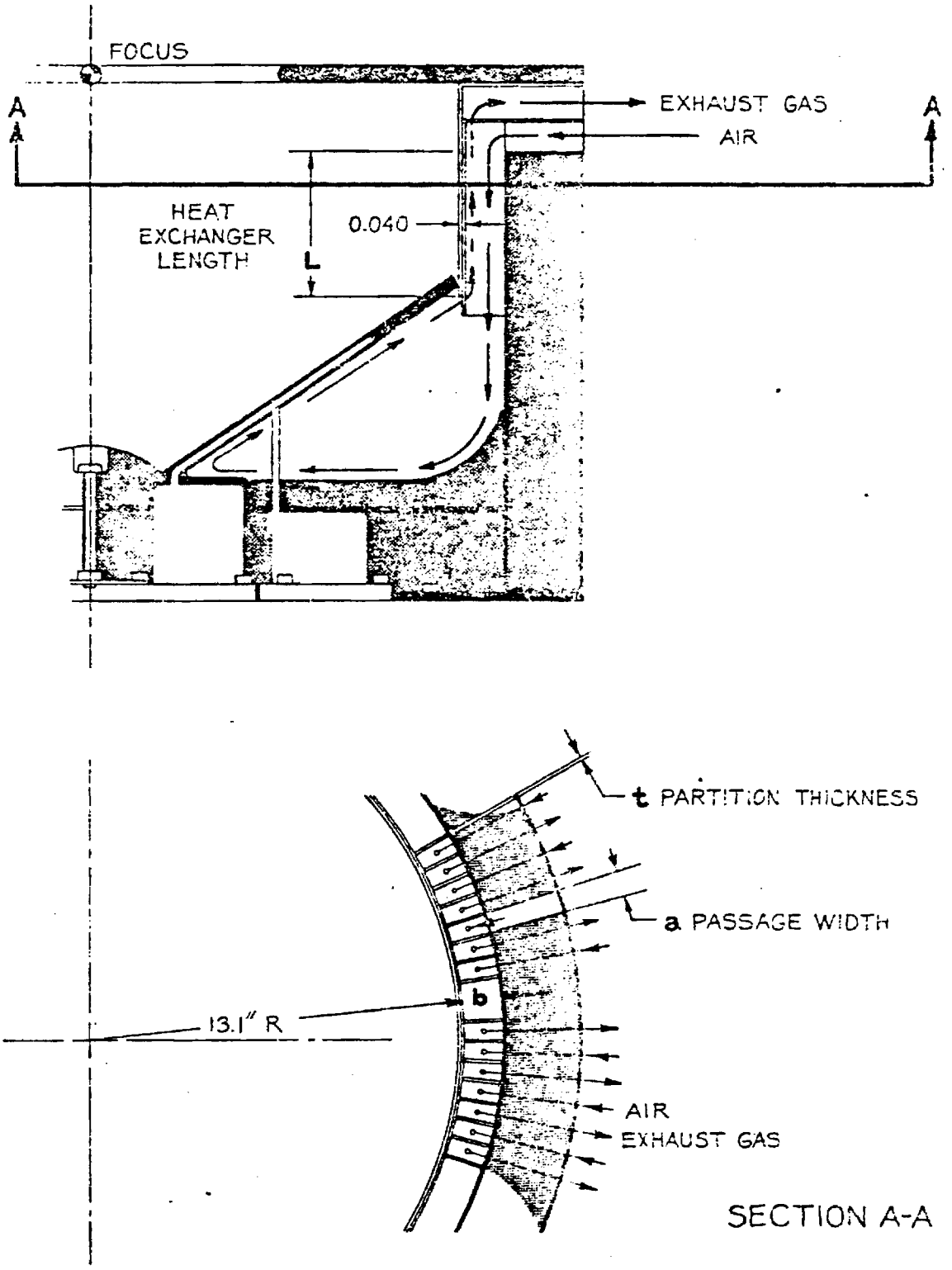

Figure 4-1. Air Preheater Design Concept

the exhaust gas to the incoming combustion air is given by the following equation:

$$q = U A_S \overline{\Delta T}$$

where

q = heat transfer rate

U = overall thermal conductance from exhaust gas to incoming air.

A_S = heat transfer area (which is the total surface area of the partitions since heat is transferred through each partition).

$\overline{\Delta T}$ = log mean temperature difference between the exhaust gas and air.

The heat transfer area is given by the number of partitions multiplied by the area of the partition.

A_S = (circumference) N (bL)

A_S = 2 (13.14 + b/2) NbL,

here N is the number of partitions per unit length around the circuference and other symbols are defined in Figure 4-1. The overall thermal conductance can be expressed as:

$$\frac{1}{U} = \left(\frac{1}{h}\right)_{air} + \left(\frac{t}{k}\right)_{partition} + \left(\frac{1}{h}\right)_{gas}$$

The h's in this expression are convective heat transfer coefficients on the air and exhaust gas sides of a partition and the other term is on the conductive thermal resistance through a partition. It is shown later in this section that the value of h is primarily a function of the gas thermal conductivity and the aspect ratio of

the passage, i.e., the ratio a/b. The value of h increases with increasing thermal conductivity and decreasing aspect ratio.

Consideration of the heat transfer equation reveals that the heat transfer rate can be increased by increasing the number of partitions. Increasing the number of partitions simultaneously increases the heat transfer area and decreases the aspect ratio. Heat transfer rates are also increased by increasing the annulus size, i.e., increasing b which produces the same effect as increasing the number of partitions.

Obviously, several combinations of annulus size, b, number of partitions, N, and partition thickness, t, can be determined for a required heat transfer rate. The following analysis shows a particular combination which results in a reasonable design.

4.1 DESIGN SPECIFICATION

The design is based on the following specifications:

Air:

Mass flow rate = 286 lbs/hr
(3825 standard cu ft/hr)

Inlet temperature = 70°F

Outlet temperature = 1400°F

Exhaust Gas:

Mass flow rate = 289 lbs/hr
(4030 standard cu ft/hr)

Inlet temperature = 1850°F

Properties of the air and the exhaust gas were assumed constant. Air properties were taken directly from published data.[7] Some of the exhaust gas properties (density and specific heat) were determined using the mass fractions of the gas composition. The exhaust gas composition was assumed to be that resulting from the burning of fuel with 10 percent excess air.

$$C H_4 + 2.2 (O_2 + 3.76N_2) \rightarrow CO_2 + 2 H_2O + 0.2 O_2 + 8.272 H_2.$$

Other properties of the exhaust gas (viscosity and thermal conductivity) were estimated from the properties of nitrogen.

4.2 FLOW CHARACTERISTICS OF THE AIR AND THE EXHAUST GAS

Characteristics of flow in the preheater are governed by the Reynolds number of the air and exhaust gas. The Reynolds number for gas flow in a passage is

$$Re \equiv \frac{\rho v \, de}{\mu}$$

or

$$Re = \frac{m}{A} \frac{de}{\mu}$$

m = mass flow rate

A = flow cross sectional area

μ = viscosity

de = an equivalent diameter

= 4 (cross-sectional area/wetted perimeter).

The equivalent diameter for a rectangular passage is given by

$$de = 2 a/(1 + \frac{a}{b}).$$

Values for flow rates and the possible number and configuration of flow passages were considered and it was found that for any expected final design the Reynolds numbers would be small. Therefore, the flow of the air and the exhaust gas in the preheater will be laminar.

The expression for pressure drop for flow in a passage is:

$$\Delta p = \frac{L}{de} \quad (4\ F) \quad \frac{\rho V^2}{2g} \ ,$$

f = fanning fraction factor

ρ = gas density

V = velocity

For laminar flow in rectangular passages of low aspect ratio, the friction factor is given by:[8]

$$f = \frac{24}{Re}$$

4.3 HEAT TRANSFER RELATIONS

For laminar flow in a rectangular passage, the convective heat transfer coefficient can be determined from Figure 4-2 which gives the Nusselt number as a function of aspect ratio (Knudsen and Katz). The Nusselt numbers given in Figure 4-2 are based on average heat transfer coefficients over passages which are long in the direction of flow. These values apply when the passage length satisfies the condition.

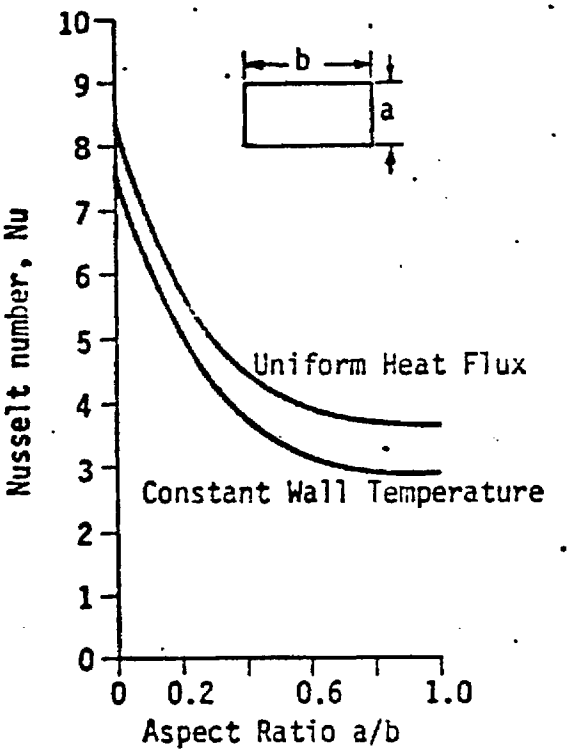

Figure 4-2. Nusselt Number for Laminar Flow in a Rectangular Duct

$$L > 0.014 \; Re \; Pr \; de,$$

where Pr is the Prandtl number of the gas and the other terms are as previously defined. An evaluation of the expected design configuration and flow conditions has shown this relationship is easily satisfied. Note that Figure 4-2 contains two curves, one for constant wall temperature and one for uniform heat flux at the wall. Since probably neither of these conditions exist in the preheater, an average value between the two was used.

In summary, for a given annulus size (b) and number of partitions (N) of thickness (t) the passage width is determined by

$$a = \frac{1}{N} - t.$$

Hence the aspect ratio (a/b) is fixed and the Nusselt number is given by Figure 4-2. The convective heat transfer coeffcient is then determined from

$$h = \frac{k}{de} \; Nu,$$

where k is the thermal conductivity of the gas.

4.4 PREHEATER DESIGN

The heat transfer in the preheater is that required to heat the incoming air from 70° to 1,400°F.

$$q = \dot{m} \; Cp \; \Delta T$$

$$q = (286)(0.254)(1,330)$$

$$q = 96,617 \text{ Btu/hr.}$$

The value of the air specific heat of 0.254 Btu/lb-°F is that corresponding to the mean air temperature of 735°F.

The above heat transfer rate applies to the exhaust gas. A trial and error procedure was used to determine the change in temperature and the mean temperature for the exhaust gas. It was found that the exhaust gas, which enters the preheater at 1,850°F is 0.309 Btu/lb-°F.

For the above entering and exit temperatures of the air and exhaust gas, the log mean temperature difference for the preheater is 565°F.

As previously stated the heat transfer equation for the preheater is

$$q = UA_s \overline{\Delta T}.$$

Substituting the above values for the heat transfer rate and the log mean temperature difference, this equation gives

$$96{,}617 = UA_s\ (565)$$

or

$$UA_s = 171 \text{ Btu/hr-°F}$$

where U = overall thermal conductance, Btu/hr-ft^2-°F

A_s = heat transfer area, ft^2

The heat transfer area was previously shown to be

$$A_s = 2\pi\ (13.14 + b/2)\ NbL.$$

Since the length L of the partitions (preheater) occurs only in this expression for the area, heat transfer rates will be directly proportional to L. The effect of the annulus size, b, is more complex since a change in b will produce a change in both the area A_s and the conductance U.

From manufacturing considerations, the thickness of the metal partitions was selected to be 0.010 inch. Figure 4-3 was constructed by assuming various values of N, the number of partitions per inch, and then determining the area A_s and the conductance U. Three values for the annulus size b were used and Figure 4-3 shows the strong influence of the variable. Only one value of L, 2.5, inch, was used since, as stated above, the curves would be shifted directly proportional to a change in this variable.

A conservative design is 1,200 total partitions (14 per inch) of length L = 2.5 inch, width b = 1 inch, and thickness T = 0.010 inch. The passage width, a, for this design will be 0.064 inch.

4.4.1 Pressure Drop and Blower Requirement

The pressure required to produce the air and exhaust gas flow through the receiver was estimated used the pressure drop equation previously given. Values used in the calculations and the results are presented in Table 4-I. It is seen that an

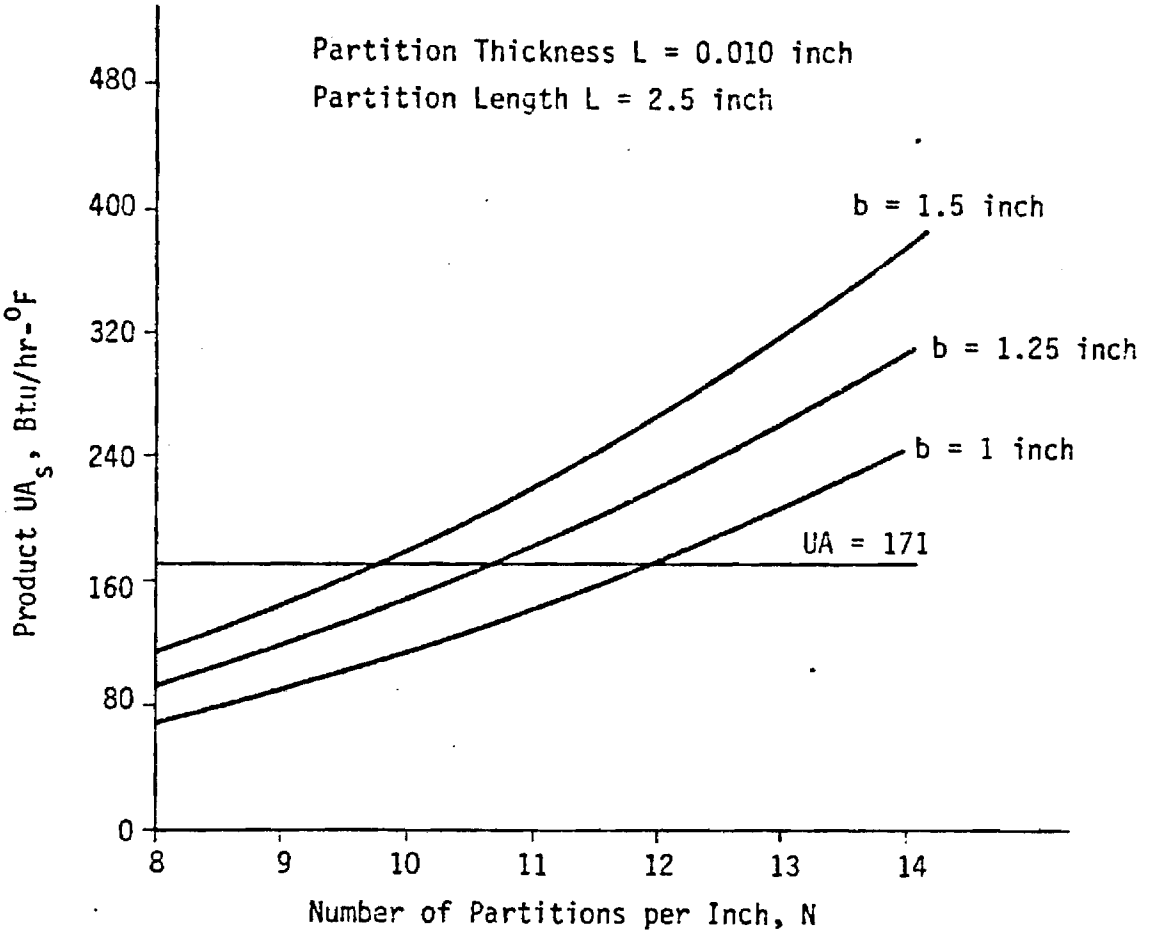

Figure 4-3. Heat Transfer in Preheater as Function of the Number of Flow Passages

Table 4-I. Pressure Drop for Air and Exhaust Gas Flow

Location	$4f\frac{L}{d}$	Density (lb/ft^3)	Velocity (ft/sec)	Pressure Drop (psi)
Air flow in Inlet Manifold	0.4	0.0748	50	0.0081
Transition from Manifold to Preheater	1.0	0.0748	50 to 4	0.0171
Air Flow in Preheater	14.6	0.0331	9	0.0042
Transition from Preheater to Combustor	0.3	0.02158	14 to 50	0.0017
Gas Flow in Combustor	--	--	--	0.2889*
Transition from Combustor to Preheater	1.0	0.01644	50 to 18	0.0018
Exhaust Gas Flow in Preheater	17.3	0.0215	14	0.0079
Transition to Exit Manifold	0.35	0.0309	10 to 120	0.017
Exhaust Gas Flow in Exit Manifold	0.4	0.0309	120	0.019
			TOTAL	0.3657

* Pressure drop estimate for gas flow in combustor supplied by Fairchild.

estimated pressure of approximately 0.4 psi is required. The power to develop this pressure is given by

$$\text{Horsepower} = (\text{pressure (C.F.M.)}/33{,}000$$
$$= (0.4 \times 144)(3{,}825/60)/33{,}000$$
$$= 0.1113$$

Assuming that the blower would have an efficiency of 50%, the total power requirment for the gas flow system is 0.223 horsepower.

4.5 HEAT LOSSES

Energy is lost from the combustor zone of the receiver by the transfer of heat through the structure to the surroundings. The heat transfer is estimated by the equation

$$q = \Delta T/R$$

where q is the heat transfer in Btu/hr, ΔT is the temperature difference between the hot gas in the combustor and the surroundings, and R is the total thermal resistance from the hot gas to the surroundings. The total thermal resistance is in general the sum of convection and conduction resistances. Convection resistance is calculated by

$$R = 1/hA$$

where h is a heat transfer coefficient and A the surface area. Conduction resistance is calculated by

$$R = t/k\ \bar{A},$$

where t is the thickness of the material in the direction of conduction, k is the material thermal conductivity, and $\bar{A}$ is the cross-sectional area through which heat is being conducted. If the cross-sectional area varies along the direction of conduction from say A_1 to A_2, then $\bar{A}$ is calculated as a log mean area by[9]

$$\bar{A} = (A_1 - A_2)/L_n(A_1/A_2).$$

For the heat transfer calculations, the combustor, as shown in Figure 4-2, can be divided into three zones. In Zone 1, heat is transferred from the hot combustion gases through the ceramic cup to the incoming preheated combustion air. Since the incoming air is mixed and burned with the gas fuel to form the hot combustion gases, heat transfer to the air is not included as an energy loss. However, the heat transfer to the air serves to further increase the incoming air temperature and energy is lost by heat transfer from the preheated air through the insulation and to the surrounding ambient air.

In Zone 2, heat is transferred from the hot combustion gases through the ceramic cup, through the insulation and to the surrounding ambient air. In Zone 3, heat is transferred from the hot combustion gases through the ceramic cup, through the insulation and into the engine structure.

An analysis performed on the combustor[10] indicates that, for the case of 10 percent excess air, the flame temperature is expected to be approximately 3100°F. The hot combustion

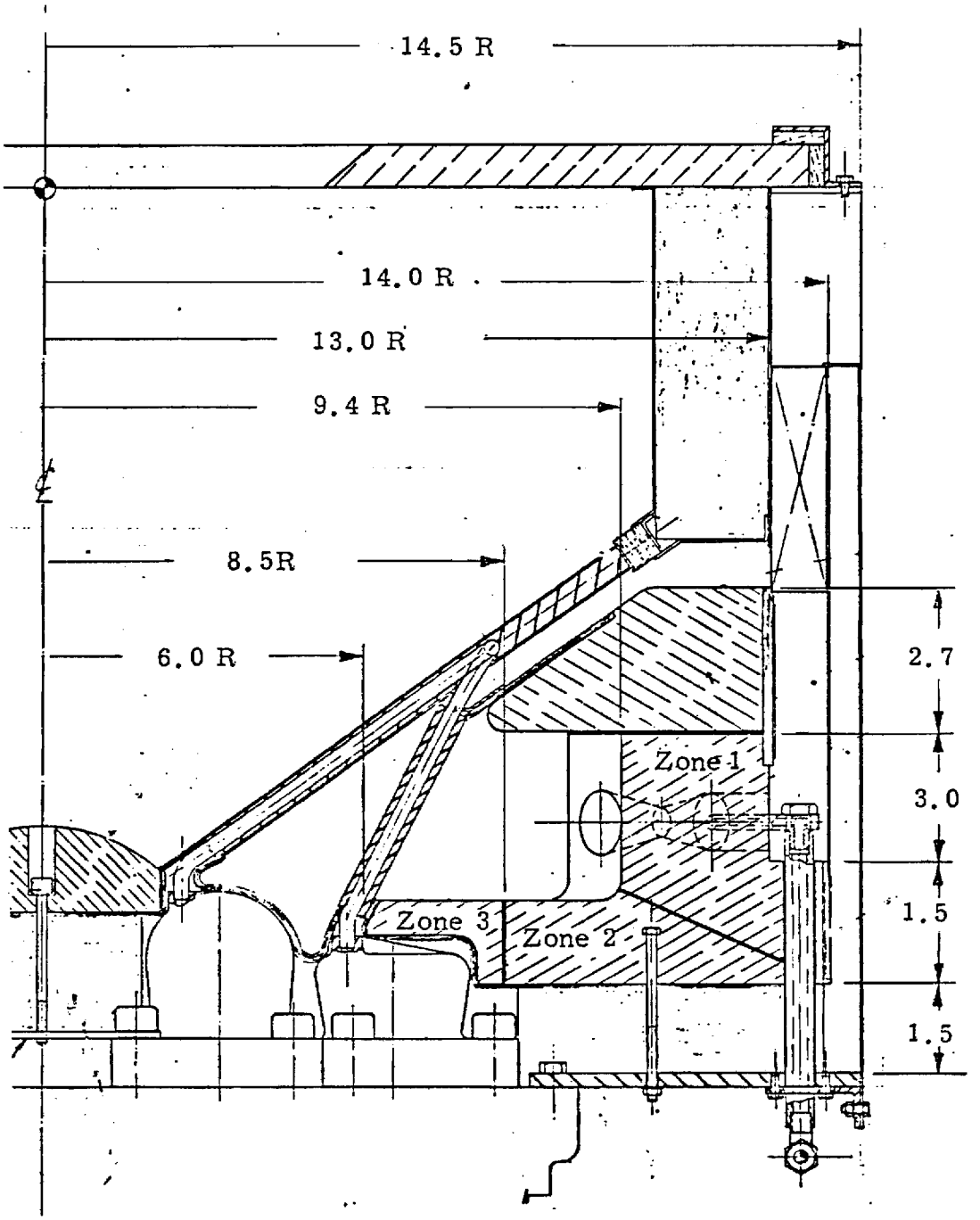

Figure 4-4. Combustor Heat Loss Transfer

gas cools to around 1830°F before exiting to the air preheater. Therefore, an average temperature of 2500°F was assumed for the hot gas. The combustion analysis also indicated that the heat coefficient for convection from the hot gas to the ceramic cup would be on the order of 50 Btu/hr-ft^2-°F; therefore, this value was assumed for the heat transfer coefficient. The heat transfer coefficients for convection between the incoming combustion air and adjacent surface, and also between the ambient air and the receiver outside surfaces, were assumed to be 20 Btu/hr-ft^2-°F. Exact material specifications for the ceramic and the insulation were not available; therefore, the thermal conductivity for the ceramic was assumed to be 2.5 Btu/hr-ft-°F (alumina) and, for the insulation, 0.05 Btu/hr-ft-°F (glass wool).

In the analysis, all of the heat transferred from the hot gas to the ceramic surface by convection was assumed to be conducted through the ceramic. In fact, part of the heat transferred to the ceramic surface by convection is radiated from the surface to the conical heat receiver surface. This radiated energy would therefore subtract from the energy loss. However, this effect was neglected in order to compensate for some additional energy loss by heat transfer to the engine structure.

4.5.1 Heat Transfer in Zone 1

The heat transfer in Zone 1, from the hot gas to the incoming combustion air, is first determined.

$$A_1 = 2\pi(9.4)(3)/144 = 1.230 \text{ ft}^2$$

$$A_2 = 2\pi(13)(3)/144 = 1.702 \text{ ft}^2$$

Convection resistance from the hot gas to the ceramic surface is

$$R = 1/(50)(1.230)$$

$$= 0.0163$$

Conduction resistance through ceramic is

$$\overline{A} = (1.702 - 1.23)/L_n\ (1.702/1.23)$$

$$= 1.453 \text{ ft}^2$$

$$R = (3.6)/(2.5)(1.453)(12)$$

$$= 0.0826$$

Convection resistance from the ceramic surface to air is

$$R = 1/(20)(1.702)$$

$$= 0.0294$$

The total resistance is the sum of these individual resistances, of 0.1283. The hot gas temperature is assumed to be 2500°F and the preheated air is at a temperature of 1400°F; therefore, the heat transfer rate is

$$q = (2500 - 1400)/0.1283$$

$$q = 8574 \text{ Btu/hr}$$

This heat serves to increase the temperature of the incoming air, which is calculated by

$$q = \dot{m}\, C_p \Delta T$$

$$8574 = (286)(0.2746)\Delta T$$

$$\Delta T = 109.$$

Therefore, the incoming air which was heated to 1400°F in the preheater will increase from heat transfer through the ceramic cone.

The energy loss in Zone 1 is that resulting from heat transfer from the air at an average temperature of 1450°F through the insulation to ambient air at a temperature of 70°F.

$$A_1 = 2\pi(14)(5.7)/144$$

$$= 3.482 \text{ ft}^2$$

$$A_2 = 2\pi(14.5)(5.7)/144$$

$$= 3.606 \text{ ft}^2$$

$$\bar{A} = \frac{3.606 - 3.482}{L_n\ (3.606/3.482)}$$

$$\bar{A} = 3.544 \text{ ft}^2$$

Convection resistance on the inside is

$$R = 1/(20)(3.482)$$

$$= 0.01436.$$

Conduction resistance through the insulation

$$R = (0.5)/(0.05)(3.544)(12)$$

$$= 0.2351$$

Convection resistance on the outside is

$$R = 1/(20)(3.606)$$
$$= 0.01386$$

The total thermal resistance is therefore 0.2633 and the heat loss in Zone 1 is

$$q_1 = (1450-70)/0.2633$$
$$q_1 = 5290 \text{ Btu/hr}$$

4.5.2 Heat Transfer in Zone 2

The heat transfer in Zone 2 is from the hot gas to the ambient air. The convection resistance from the hot gas to the ceramic core is

$$A_1 = [\pi(9.4)^2 - \pi(8.5)^2]/144$$
$$= 0.3515 \text{ ft}^2$$
$$R = 1/(30)(0.3515)$$
$$= 0.0569.$$

The conduction resistance through the ceramic cone is

$$A_2 = [\pi(14.5)^2 - \pi(8.5)^2]/144$$
$$= 3.017$$
$$\bar{A} = (3.0107 - 0.3515)/L_n(3.0107/0.3515)$$
$$= 1.238 \text{ ft}^2$$
$$R = (1.5)/(0.5)(1.2382)(12)$$
$$= 0.0404.$$

Conduction resistance through the insulation is

$$R = (1.5)/(0.05)(3.0107)(12)$$
$$= 0.8304$$

Convection resistance to the ambient air is

$$R = 1/(20)(3.0107)$$
$$= 0.0569.$$

The total resistance is then 0.9443 and the heat loss in Zone 2 is

$$q_2 = (2500-70)/0.9443$$
$$q_2 = 2573 \text{ Btu/hr.}$$

4.5.3 Heat Transfer in Zone 3

The heat transfer in Zone 3 is from the hot gas to the engine structure.

$$A = [\pi(8.5)^2 - \pi(6)^2]/144$$
$$= 0.7909 \text{ ft}^2$$

Convection resistance from the hot gas to the ceramic cone is

$$R = 1/(50)(0.7909)$$
$$= 0.0253.$$

Conduction resistance through the ceramic is

$$R = (0.6)/(2.5)(0.7909)(12)$$
$$= 0.0253$$

Conduction resistance through the insulation is

$$R = (0.3)/(0.05)(0.7905)(12)$$
$$= 0.6322.$$

The total thermal resistance is therefore 0.6828 and the heat loss in Zone 3 (assuming the engine structure to be at 500°F) is

$$q_3 = (2500-500)/0.6828$$
$$q_3 = 2929 \text{ Btu/hr.}$$

Total heat loss from the combustion is the sum of q_1, q_2, q_3, or 10,792 Btu/hr.